UAV Waypoint Opportunistic Navigation in GNSS-Denied Environments

YANHAO YANG, Student Member, IEEE
Carnegie Mellon University, Pittsburgh, PA USA

JOE KHALIFE, Member, IEEE
University of California Irvine, CA USA

JOSHUA J. MORALES, Member, IEEE
University of California Irvine, CA USA

ZAHER M. KASSAS, Senior Member, IEEE
University of California Irvine, CA USA

Navigation of an unmanned aerial vehicle (UAV) to reach a desired waypoint with provable guarantees in global navigation satellite system (GNSS)-denied environments is considered. The UAV is assumed to have an unknown initial state (position, velocity, and time) and the environment is assumed to possess multiple terrestrial signals of opportunity (SOPs) transmitters with unknown states (position and time) and one anchor SOP whose states are known. The UAV makes pseudorange measurements to all SOPs to estimate its own states simultaneously with the states of the unknown SOPs. The waypoint navigation problem is formulated as a greedy (i.e., one-step look-ahead) multiobjective motion planning (MOMP) strategy, which guarantees that the UAV gets to within a user-specified distance of the waypoint with a user-specified confidence. The MOMP strategy balances two objectives: i) navigating to the waypoint; and (ii) reducing UAV's position estimate uncertainty. It is demonstrated that in such an environment, formulating the waypoint navigation problem in a so-called "naive" fashion by heading directly to the waypoint would result in failing to reach the waypoint. This is due to poor estimability of the environment. In contrast, the MOMP strategy guarantees (in a probabilistic sense) reaching the waypoint. Monte Carlo simulation results are presented showing that the MOMP strategy achieves the desired objective with 95% success rate compared to a 36% success rate with the naive approach. Experimental results are presented for a UAV navigating to a waypoint in a cellular SOP environment, where the MOMP strategy successfully reaches the waypoint, while the naive strategy fails to do so.

I. INTRODUCTION

Unmanned vehicles (UAVs) are increasingly being used in a wide range of civilian and military applications, in which it is too costly or dangerous to send human-operated vehicles. These applications include search and rescue, fire fighting, traffic monitoring, agriculture, delivery, and surveillance. The majority of missions in these applications require the UAV to fly to specified waypoints efficiently and reliably in dynamic and uncertain environments. Reaching these waypoints reliably with *no* human-in-the-loop requires the UAV to continuously maintain its position in space and time within the environment using an accurate and robust navigation system.

Today's UAV navigation systems essentially rely on global navigation satellite system (GNSS) signals. However, it is well-known that GNSS signals can become unreliable in environments where UAVs conduct missions: GNSS signals get highly attenuated in deep urban canyons and under canopies [1] and are susceptible to jamming and malicious spoofing [2]. To alleviate these shortcomings during GNSS outages, UAV navigation systems typically supplement GNSS receivers with additional sensors (e.g., inertial measurement units (IMUs) [3], cameras [4], and lasers [5]). However, after prolonged GNSS unavailability periods, the UAV's position estimation error and estimation uncertainty could accumulate to unacceptable levels, compromising the safety and success of the UAV's mission. While the accumulation rate of UAV positioning error could be reduced by incorporating additional sensors into the UAV's sensor-suite, this could violate cost, size, weight, and power (CSWaP) constraints.

A more elegant and CSWaP-efficient approach is to detect and map existing features in the unknown environment and to prescribe the UAV's trajectory to minimize the UAV's states uncertainty, which is estimated using measurements drawn from the mapped features [6]. Fortunately, there is plenitude of features in locales of interest, which a UAV may exploit in the absence of GNSS signals in order to *autonomously* navigate to the waypoint (e.g., trees, light poles, buildings, etc.). This is typically achieved via the well-studied problem of simultaneous localization and mapping (SLAM) [7]–[9] in the robotics literature.

Another class of features, which could be exploited in GNSS-denied environments is signals of opportunity (SOPs) [10]–[12]. SOPs are ambient radio signals, which are not intended as navigation sources, e.g., cellular signals [13]–[17], digital television signals [18], [19], AM/FM

Manuscript received April 7, 2021; revised July 29, 2021; released for publication August 2, 2021. Date of publication August 10, 2021; date of current version February 10, 2022.

DOI. No. 10.1109/TAES.2021.3103140

Refereeing of this contribution was handled by J. Seo.

This work was supported in part by the National Science Foundation (NSF) under Grant 1929571 and Grant 1929965, in part by the Office of Naval Research (ONR) under Grant N00014-19-1-2613, and in part by the University of California, Irvine Multidisciplinary Engineering Research Initiative program.

Authors' addresses: Yanhao Yang is with the Mechanical Engineering Department, Carnegie Mellon University, Pittsburgh, PA 15213 USA, E-mail: (yanhaoy@andrew.cmu.edu); Joe Khalife and Zaher M. Kassas are with the Department of Mechanical and Aerospace Engineering, University of California, Irvine, CA 92697 USA E-mail: (khalifej@uci.edu; zkassas@ieee.org); Joshua J. Morales is with the Department of Electrical Engineering and Computer Science, University of California, Irvine, CA 92697 USA, E-mail: (joshum9@uci.edu). *(Corresponding author: Zaher M. Kassas.)*.

radio signals [20], [21], and low earth orbit satellite (LEO) signals [22]–[25]. SOPs have been exploited to produce navigation solutions in a standalone fashion or as an aiding source for an INS in the absence of GNSS signals [26]. Meter-level accurate navigation has been demonstrated on ground vehicles with terrestrial cellular and television SOPs [27]–[29], while submeter-level accurate navigation has been demonstrated on UAVs [30].

The problem of navigating with unknown SOPs is termed radio SLAM [26] or variations thereof [31]. While the radio SLAM problem shares similarities with the robotics SLAM problem, radio SLAM possesses specific complexities due to the dynamic and stochastic nature of the spatiotemporal state space. In particular, unlike the *static* features comprising the robotics SLAM environment, SOPs are equipped with non-ideal clocks, whose error (bias and drift) is *dynamic* and *stochastic*. What is more, the number of SOPs could be limited compared to the plenitude of static features in the robotics SLAM environment, and the initial uncertainty around the SOP states could be large. This makes the radio SLAM environment poorly estimable, and the coupling between the control objective (motion planning toward the waypoint) and sensing/estimation objective (motion planning to gather the "best" information from SOPs) evermore important. Even for the simple objective of achieving situational awareness in these environments (i.e., estimating the UAV's states simultaneously with estimating the SOPs' states) without requiring the UAV to reach a desired waypoint, it was shown that moving in a random or an open-loop fashion would cause the UAV to get lost (exhibited by filter divergence) [32].

Initial work on greedy (i.e., one-step look-ahead) motion planning for optimal information gathering in radio SLAM environments was conducted in [32], and receding horizon (i.e., multistep look-ahead) trajectory optimization was studied in [33]. While the proposed approaches were shown to maintain localization accuracy and map quality by prescribing optimal trajectories, they did not take into consideration a desired waypoint as part of the UAV's mission. Waypoint navigation brings a second objective that could *contradict* with the objective of maintaining a good estimate of the UAV's states. In contrast to previous work, this article considers the problem of UAV greedy motion planning in a radio SLAM environment to reach a desired waypoint with provable guarantees.

The contributions of this article are as follow. First, a multiobjective motion planning (MOMP) strategy is formulated. Three cost functions that reflect the two objectives—namely, mission completion and uncertainty reduction; are derived using probabilistic and information theoretic metrics. It is shown that under certain conditions, these cost functions are equivalent. Second, the cost function is modified by introducing weights for the terms pertaining to each objective, and a method to adaptively set the weights online is proposed. This adaptation is shown to be essential for successful mission completion. Third, the article identifies a stopping criterion that guarantees that the UAV is within a desired distance to the waypoint with a desired confidence, declaring the mission as complete. Fourth, Monte Carlo simulations are presented showing that the MOMP strategy achieves the desired objective with 95% success rate compared to a 36% success rate with a naive approach (i.e., one which prescribes the shortest trajectory to the waypoint without considering the UAV's position uncertainty). Fifth, experimental results are presented for a UAV navigating to a waypoint in a cellular SOP environment, where the MOMP strategy successfully reaches the waypoint, while the naive strategy fails to do so.

The rest of this article is organized as follows. Section II summarizes relevant work in the literature. Section III formulates the MOMP problem and describes the dynamics model of the UAV and SOPs, the measurement model, and the estimator model. Section IV develops the proposed MOMP strategy. Section V presents simulation results comparing naive and MOMP strategies. Section VI presents experimental results of a UAV exploiting signals from unknown cellular SOP transmitters to navigate to a waypoint using the MOMP strategy. Finally, Section VII concludes this article.

II. RELATED WORK

Waypoint navigation has been widely studied over the last decade with the development of autonomous aerial vehicles [34] and mobile robots [35]. To achieve better performance in waypoint navigation, GPS-based control systems were adopted, whether in a stand-alone fashion [36] or in a differential fashion with an inertial navigation system (INS) [37]. Other approaches relied on fusing measurements from an omnidirectional camera and a laser rangefinder in a Kalman filter for outdoor waypoint navigation [38]. The waypoint navigation problem has been formulated as an optimal control problem [39], which could be solved by linear quadratic regulator (LQR) [40], genetic algorithm [41], or a combination of local and global planning [42]. When the optimization problem becomes multiobjective, particle swarm optimization [43], or Pareto-optimality [44] has been adopted. Although the aforementioned methods achieved accurate waypoint navigation, they did not take into account the effect of motion on the estimation performance. The effect of having large estimation error in waypoint navigation may have detrimental consequences.

Motion planning approaches that optimize the path length toward a waypoint, while taking into account sensor uncertainties have been investigated in recent literature. However, sensors can provide either local or global information of the vehicle's position. In the case of the former, the motion planning algorithm accounts for the sensor uncertainty instead of optimizing for sensor uncertainty [45], [46]. In the case of the latter, path planning is affected by the predicted quality of the navigation solution which changes throughout the environment. Ray-tracing approaches for path planning were used to improve channel characterization and enhance positioning performance for autonomous ground vehicles [47]–[50] or UAVs [51]–[53], navigating with GNSS and/or SOPs. In [54], a method to predict the state uncertainty of a UAV in the presence of uncertain GNSS positioning biases using stochastic reachability analysis was proposed. A framework that guarantees that the estimation error remains less than the safety threshold for ground vehicles while navigating toward a waypoint was presented in [55]. While effective, these approaches rely on known maps to precalculate the cost function and perform optimization.

In robotics, sample-based approaches using the belief space of the robot's states are common for motion planning involving uncertainty from localization and motion. One of the sample-based methods for waypoint reaching that considers state uncertainties is the belief roadmap [56], which builds a probabilistic roadmap in a robot's state space. It propagates beliefs over the roadmap using an extended Kalman filter (EKF) and plans a path of minimum goal-state uncertainty. A modification of the sampling method was proposed by [57] in which minimizing the maximum value of its uncertainty metric encountered during the traversal of a path to make it more efficient, while intermittent sensing was considered in [58]. This approach was extended by taking visual-inertial sensing and laser scanners into consideration in [59] and [60], respectively. A rollout-policy-based algorithm enabling online replanning in an efficient manner in belief space to achieve simultaneous localization and planning in dynamic environments with the presence of large disturbances was proposed in [61]. However, for these sample-based approaches, the sampling method and numerical burden significantly affect efficiency and performance, as they require the calculation and evaluation of all the potential paths between the start point and the destination in each round. Several approaches in the literature formulated the planning as an optimization problem, constrained by uncertainty. For example, the sampled paths were constrained by the estimated error covariance in [62]. Similarly, [63] applied this constraint in particle swarm optimization to find the optimal paths satisfying the covariance bound. Localizability was also adopted as a constraint to determine possible regions and the path length was optimized within these regions for a an autonomous vehicle [64]. Although this paradigm is formulated as a constrained optimization problem, the existence of an optimal solution is *not* always guaranteed, as the constraint may contradict the primary goal. In contrast to previous work, this article considers opportunistic waypoint navigation in a GNSS-denied via radio SLAM. To achieve this objective, the article formulates a computationally efficient MOMP strategy, which guarantees (in a probabilistic sense) reaching the waypoint.

III. PROBLEM FORMULATION AND MODEL DESCRIPTION

This section formulates the MOMP problem, describes the control system model of the UAV, presents the dynamics and measurement model of the UAV and SOPs, and discusses the EKF model for estimating the UAV's and SOPs' states.

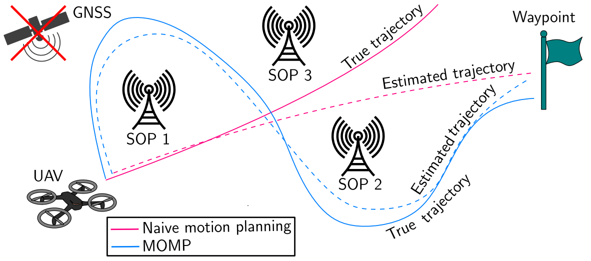

Fig. 1. UAV is deployed into an uncertain position in a GNSS-denied environment and is tasked with navigating to a waypoint. A naive strategy (shown in purple) would have the UAV move directly to the waypoint position, risking large position estimation errors, which would cause missing the waypoint. A MOMP strategy (shown in blue) would have the UAV prescribe a more complex trajectory, which balances two objectives to maintain a reliable position estimate: 1) moving to the waypoint; and 2) minimizing the UAV position uncertainty. The MOMP strategy guarantees (in a probabilistic sense) reaching the waypoint.

A. Problem Formulation

This article extends previous work on motion planning by developing a MOMP strategy for a UAV navigating with unknown SOPs, which balances two objectives: 1) navigating to a waypoint; and 2) minimizing UAV's position uncertainty. The following problem is considered. A UAV has been dropped into a GNSS-denied environment with minimal *a priori* knowledge of its own states. As shown in Fig. 1, the environment consists of multiple unknown SOPs, from which the UAV draws and fuses pseudoranges in order to estimate its own states and the states of the unknown SOPs through an EKF. The UAV is tasked with navigating to a waypoint position and is required to arrive at the waypoint within a specified distance with a specified confidence. The estimation uncertainty is heavily dependent on the relative geometry between the UAV and the SOPs. Therefore, the trajectory taken by the UAV to arrive at the waypoint affects the uncertainty in its position estimate along the way. When the uncertainty is very large, the EKF risks diverging, which in turn causes the UAV to move away from the waypoint, as illustrated in Fig. 1. To avoid such behavior, a more complex trajectory is designed to maintain a small uncertainty along the UAV trajectory, which guarantees to reach the waypoint. This is also illustrated in Fig. 1. Section IV develops the MOMP strategy.

B. UAV Control System Model

This article considers motion planning for quadrotor UAVs. Typical quadrotor controllers require full state feedback, which consists of the UAV's three-dimensional (3-D) pose (3-D position and orientation) and its first time derivative (3-D linear and angular velocities). UAVs are typically equipped with a suite of sensors to perform pose estimation, mainly a GNSS receiver, IMU, barometric pressure sensor or altimeter, magnetometer, etc. It is worth noting that UAVs rely mainly on GNSS to produce a position estimate in a global frame, e.g., earth-centered earth-fixed (ECEF) frame. In GNSS-denied environments, if equipped with the right receivers, the UAV may draw pseudorange

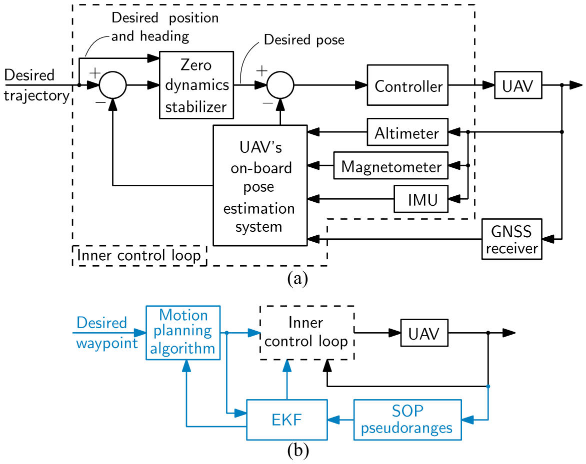

Fig. 2. High-level block diagram of the UAV control system. (a) Inner control loop consists of a standard UAV control loop, where the desired tracking position and heading angle trajectories are defined by the user. A zero dynamics stabilizer block synthesizes the tracking trajectories for the remaining states. (b) In the case of GNSS unavailability (note the absence of the GNSS receiver), the UAV can rely on SOP measurements to maintain a position estimate in a global frame. Moreover, motion planning could be performed to efficiently navigate to a desired waypoint. The additional blocks pertaining to the proposed motion planning framework for navigating with SOPs are shown in blue. It is important to note that the proposed approach is in a fashion where 1) no modifications are needed for the inner control loop; and 2) the proposed motion planning algorithm automatically computes the desired trajectories that are input to the inner control loop.

measurements from ambient SOPs to produce a position estimate in the global frame. As mentioned in the Introduction, the uncertainty associated with the SOP-based position estimate heavily depends on the relative geometry between the UAV and the SOPs. Therefore, in order to reduce this uncertainty, a motion planning algorithm is developed to reach the waypoint with a desired confidence. In addition to state feedback, a desired trajectory is required to perform UAV pose control. Zero dynamics stabilization methods were proposed to synthesize full state desired trajectories from desired position and heading trajectories only [65]. Treating the UAV controller as a black box, the proposed framework aims at the following: 1) replacing the GNSS receiver with an EKF estimating the UAV position using SOP pseudoranges; and 2) perform motion planning to determine the desired position and heading trajectories that will be passed as an input to the UAV's control system. A high-level block diagram of a typical UAV control system and the proposed system are shown in Fig. 2. Since the proposed framework uses the UAV's control system as a black box, the EKF estimating the UAV's state from SOP pseudoranges is formulated independently of the UAV's on-board control system. The UAV dynamics model assumed by the EKF is discussed next.

C. UAV Dynamics Model

For simplicity, this article assumes a planar environment. Extensions to three-dimensions are straightforward. Such extension would yield poor estimability of the UAV's vertical position due to poor geometric diversity of the SOPs' heights. In such case, other sensors (e.g., altimeter) could be readily used.

The state vector of the UAV $\boldsymbol{x}_{\mathrm{r}}$ is defined as

$$\boldsymbol{x}_{\mathrm{r}} \triangleq \left[\boldsymbol{x}_{\mathrm{pv}}^{\mathsf{T}},\ \boldsymbol{x}_{\mathrm{clk,r}}^{\mathsf{T}}\right]^{\mathsf{T}},\ \boldsymbol{x}_{\mathrm{pv}} \triangleq \left[\boldsymbol{r}_{\mathrm{r}}^{\mathsf{T}},\ \dot{\boldsymbol{r}}_{\mathrm{r}}^{\mathsf{T}}\right]^{\mathsf{T}},\ \boldsymbol{x}_{\mathrm{clk,r}} \triangleq \left[\delta t_{\mathrm{r}},\ \dot{\delta t}_{\mathrm{r}}\right]^{\mathsf{T}}$$

where $\boldsymbol{r}_{\mathrm{r}} \in \mathbb{R}^2$ and $\dot{\boldsymbol{r}}_{\mathrm{r}} \in \mathbb{R}^2$ are the UAV's 2-D position and velocity, respectively; and $\delta t_{\mathrm{r}} \in \mathbb{R}$ and $\dot{\delta t}_{\mathrm{r}} \in \mathbb{R}$ are the UAV-mounted receiver's clock bias and drift, respectively. The UAV's position and velocity states $\boldsymbol{x}_{\mathrm{pv}}$ will be assumed to evolve according to a 2-D planar motion model [66]. Taking the omnidirectional flying ability of the multirotor into consideration, the UAV's *nominal* continuous-time control input vector $\boldsymbol{u}_{\mathrm{r}}$, is given by

$$\boldsymbol{u}_{\mathrm{r}_c} \triangleq [a_c,\ \theta_c]^{\mathsf{T}}$$

where $a_c \in \mathbb{R}^+$ and $\theta_c \in [-\pi, \pi)$ are the continuous-time absolute acceleration and corresponding heading angle, respectively. Note that $\boldsymbol{u}_{\mathrm{r}_c}$ is not the actual control input applied to the UAV, but is the control input computed by the motion planning algorithm from which the desired 2-D position and heading can be computed and input to the UAV controller, as shown in Fig. 2(b). The desired altitude is set to be constant. Due to actuation errors and process noise, the *actual* continuous-time control input vector will be

$$\bar{\boldsymbol{u}}_{\mathrm{r}_c} = \boldsymbol{u}_{\mathrm{r}_c} + \tilde{\boldsymbol{u}}_{\mathrm{r}_c} \triangleq \left[\bar{a}_c,\ \bar{\theta}_c\right]^{\mathsf{T}}$$

where $\tilde{\boldsymbol{u}}_{\mathrm{r}_c} \triangleq [\tilde{a}_c, \tilde{\theta}_c]^{\mathsf{T}}$, and $\tilde{a}_c$ and $\tilde{\theta}_c$ are uncorrelated, zero-mean, white random processes with power spectra $\tilde{q}_a$ and $\tilde{q}_\theta$, respectively. The continuous-time state-space model of the UAV's position and velocity is formulated as

$$\begin{aligned} \dot{\boldsymbol{x}}_{\mathrm{pv}}(t) &= \mathbf{A}_{\mathrm{pv}}\boldsymbol{x}_{\mathrm{pv}}(t) + \mathbf{B}_{\mathrm{pv}}\boldsymbol{g}_{\mathrm{r}}[\bar{\boldsymbol{u}}_{\mathrm{r}_c}(t)] \\ \mathbf{A}_{\mathrm{pv}} &\triangleq \begin{bmatrix} \mathbf{0}_{2\times 2} & \mathbf{I}_{2\times 2} \\ \mathbf{0}_{2\times 2} & \mathbf{0}_{2\times 2} \end{bmatrix}, \quad \mathbf{B}_{\mathrm{pv}} \triangleq \begin{bmatrix} \mathbf{0}_{2\times 2} \\ \mathbf{I}_{2\times 2} \end{bmatrix} \end{aligned} \tag{1}$$

$$\boldsymbol{g}_{\mathrm{r}}[\bar{\boldsymbol{u}}_{\mathrm{r}_c}(t)] \triangleq \left[\bar{a}_c(t)\cos[\bar{\theta}_c(t)],\ \bar{a}_c(t)\sin[\bar{\theta}_c(t)]\right]^{\mathsf{T}}$$

where $\mathbf{0}_{2\times 2} \in \mathbb{R}^{2\times 2}$ is a matrix zeros and $\mathbf{I}_{2\times 2} \in \mathbb{R}^{2\times 2}$ is the identity matrix. Since the actual control input is unknown, the function $\boldsymbol{g}_{\mathrm{r}}[\bar{\boldsymbol{u}}_{\mathrm{r}}(t)]$ in (1) is linearized around the nominal input $\boldsymbol{u}_{\mathrm{r}}(t)$, yielding

$$\begin{aligned} \boldsymbol{g}_{\mathrm{r}}[\bar{\boldsymbol{u}}_{\mathrm{r}_c}(t)] &\approx \boldsymbol{g}_{\mathrm{r}}[\boldsymbol{u}_{\mathrm{r}_c}(t)] + \tilde{\mathbf{D}}_{\mathrm{r}}(t)\tilde{\boldsymbol{u}}_{\mathrm{r}_c}(t) \\ \tilde{\mathbf{D}}_{\mathrm{r}}(t) &\triangleq \begin{bmatrix} \cos[\theta_c(t)] & -a_c(t)\sin[\theta_c(t)] \\ \sin[\theta_c(t)] & a_c(t)\cos[\theta_c(t)] \end{bmatrix} \end{aligned} \tag{2}$$

where $\tilde{\mathbf{D}}_{\mathrm{r}}(t)$ is the Jacobian matrix of $\boldsymbol{g}_{\mathrm{r}}[\bar{\boldsymbol{u}}_{\mathrm{r}_c}(t)]$ with respect to $\bar{\boldsymbol{u}}_{\mathrm{r}_c}(t)$. Combining (1) and (2) and discretizing at a sampling interval T assuming zero-order hold of the control input (i.e., $\{\boldsymbol{u}_{\mathrm{r}_c}(t) = \boldsymbol{u}_{\mathrm{r}_c}(kT) \triangleq \boldsymbol{u}_{\mathrm{r}}(k), kT \leq t < (k+1)T\}$), the discrete-time UAV's position and velocity states can be modeled as

$$\boldsymbol{x}_{\mathrm{pv}}(k+1) = \mathbf{F}_{\mathrm{pv}}\boldsymbol{x}_{\mathrm{pv}}(k) + \boldsymbol{\Gamma}_{\mathrm{pv}}\boldsymbol{g}_{\mathrm{r}}\left[\boldsymbol{u}_{\mathrm{r}}(k)\right] + \boldsymbol{w}_{\mathrm{pv}}(k),\ k = 0, 1, \ldots$$

$$\mathbf{F}_{\mathrm{pv}} \triangleq \begin{bmatrix} \mathbf{I}_{2\times 2} & T\mathbf{I}_{2\times 2} \\ \mathbf{0}_{2\times 2} & \mathbf{I}_{2\times 2} \end{bmatrix}, \quad \mathbf{\Gamma}_{\mathrm{pv}} \triangleq \begin{bmatrix} \frac{T^2}{2}\mathbf{I}_{2\times 2} \\ T\mathbf{I}_{2\times 2} \end{bmatrix}, \quad \boldsymbol{u}_{\mathrm{r}}(k) \triangleq \begin{bmatrix} a(k) \\ \theta(k) \end{bmatrix} \tag{3}$$

where $a(k) \triangleq a_c(kT)$ and $\theta(k) \triangleq \theta_c(kT)$, and $\boldsymbol{w}_{\mathrm{pv}}(k)$ is the discretized process noise vector, which is a zero-mean white sequence with covariance $\mathbf{Q}_{\mathrm{pv}}(k)$ given by

$$\mathbf{Q}_{\mathrm{pv}}(k) = \begin{bmatrix} \frac{T^3}{3}\mathbf{Q}_c(k) & \frac{T^2}{2}\mathbf{Q}_c(k) \\ \frac{T^2}{2}\mathbf{Q}_c(k) & T\mathbf{Q}_c(k) \end{bmatrix} \tag{4}$$

$$\mathbf{Q}_c(k) \triangleq \mathbf{D}_{a,\theta}(k)\mathbf{Q}_{a,\theta}\mathbf{D}^{\mathsf{T}}_{a,\theta}(k), \quad \mathbf{Q}_{a,\theta} = \mathrm{diag}\left[\tilde{q}_a,\ \tilde{q}_\theta\right] \tag{5}$$

$$\mathbf{D}_{a,\theta}(k) \triangleq \tilde{\mathbf{D}}_{a,\theta}(kT) = \begin{bmatrix} \cos[\theta(k)] & -a(k)\sin[\theta(k)] \\ \sin[\theta(k)] & a(k)\cos[\theta(k)] \end{bmatrix}. \tag{6}$$

Furthermore, as in all practical systems, the UAV's acceleration and velocity are constrained according to

$$\begin{cases} a(k) \leq a_{\mathrm{r,max}} \\ \|\dot{\boldsymbol{r}}_{\mathrm{r}}(k)\|_2 \leq v_{\mathrm{r,max}} \end{cases} \tag{7}$$

which, for $\boldsymbol{e} \triangleq [1 \quad 0]^{\mathsf{T}}$, can also be expressed as

$$\begin{cases} \left(\boldsymbol{e}^{\mathsf{T}}\boldsymbol{u}_{\mathrm{r}}(k)\right)^2 \leq a^2_{\mathrm{r,max}} \\ \left\|\boldsymbol{g}_{\mathrm{r}}\left[\boldsymbol{u}_{\mathrm{r}}(k)\right] + \frac{1}{T}\dot{\boldsymbol{r}}_{\mathrm{r}}(k)\right\|_2^2 \leq \left(\frac{1}{T}v_{\mathrm{r,max}}\right)^2. \end{cases} \tag{8}$$

The UAV-mounted receiver's clock state $\boldsymbol{x}_{\mathrm{clk,r}}$ is modeled according to the standard double integrator model driven by process noise, whose discrete-time dynamics are given by

$$\boldsymbol{x}_{\mathrm{clk,r}}(k+1) = \mathbf{F}_{\mathrm{clk}}\boldsymbol{x}_{\mathrm{clk,r}}(k) + \boldsymbol{w}_{\mathrm{clk,r}}(k), \quad k = 0, 1, 2, \ldots \tag{9}$$

where $\boldsymbol{w}_{\mathrm{clk,r}}$ is a zero-mean white noise sequence with covariance $\mathbf{Q}_{\mathrm{clk,r}}$ given by

$$\mathbf{F}_{\mathrm{clk}} = \begin{bmatrix} 1 & T \\ 0 & 1 \end{bmatrix}, \quad \mathbf{Q}_{\mathrm{clk,r}} = \begin{bmatrix} S_{\tilde{w}_{\delta t_{\mathrm{r}}}}T + S_{\tilde{w}_{\dot{\delta} t_{\mathrm{r}}}}\frac{T^3}{3} & S_{\tilde{w}_{\dot{\delta} t_{\mathrm{r}}}}\frac{T^2}{2} \\ S_{\tilde{w}_{\dot{\delta} t_{\mathrm{r}}}}\frac{T^2}{2} & S_{\tilde{w}_{\dot{\delta} t_{\mathrm{r}}}}T \end{bmatrix}$$

where $S_{\tilde{w}_{\delta t_{\mathrm{r}}}}$ and $S_{\tilde{w}_{\dot{\delta} t_{\mathrm{r}}}}$ are the power spectra of the continuous-time white process noise driving the evolution of the clock bias and drift, which are approximated with the frequency random walk coefficient $h_{-2,\mathrm{r}}$ and the white frequency coefficient $h_{0,\mathrm{r}}$, leading to $S_{\tilde{w}_{\delta t_{\mathrm{r}}}} \approx \frac{h_{0,\mathrm{r}}}{2}$ and $S_{\tilde{w}_{\dot{\delta} t_{\mathrm{r}}}} \approx 2\pi^2 h_{-2,\mathrm{r}}$.

Combining (3) and (9) yields the discrete-time dynamics of the UAV's state vector $\boldsymbol{x}_{\mathrm{r}}$, which is given by

$$\boldsymbol{x}_{\mathrm{r}}(k+1) = \mathbf{F}_{\mathrm{r}}\boldsymbol{x}_{\mathrm{r}}(k) + \mathbf{\Gamma}_{\mathrm{r}}\boldsymbol{g}_{\mathrm{r}}[\boldsymbol{u}_{\mathrm{r}}(k)] + \boldsymbol{w}_{\mathrm{r}}(k), \quad k = 0, 1, 2, \ldots$$

$$\mathbf{F}_{\mathrm{r}} \triangleq \mathrm{diag}\left[\mathbf{F}_{\mathrm{pv}},\ \mathbf{F}_{\mathrm{r}}\right], \quad \mathbf{\Gamma}_{\mathrm{r}} \triangleq \left[\mathbf{\Gamma}^{\mathsf{T}}_{\mathrm{pv}},\ \mathbf{0}_{2\times 2}\right]^{\mathsf{T}} \tag{10}$$

and $\boldsymbol{w}_{\mathrm{r}} \triangleq [\boldsymbol{w}^{\mathsf{T}}_{\mathrm{pv}}, \boldsymbol{w}^{\mathsf{T}}_{\mathrm{clk,r}}]^{\mathsf{T}}$ is the overall process noise covariance, which is a zero-mean white sequence with covariance

$$\mathbf{Q}_{\mathrm{r}} = \mathrm{diag}\left[\mathbf{Q}_{\mathrm{pv}},\ \mathbf{Q}_{\mathrm{clk,r}}\right].$$

D. SOP Dynamics Model

The environment consists of one fully known anchor SOP, denoted with a subscript a, and m unknown SOPs. To satisfy the observability condition established in [33] and [67], the knowledge of the state vector of the anchor SOP, denoted $\boldsymbol{x}_{\mathrm{s}_{\mathrm{a}}}$, is assumed. Note that the UAV's control inputs $\boldsymbol{u}_{\mathrm{r}}$ are with respect to a global coordinate frame in which the SOPs are expressed. This requires the UAV to have *a priori* knowledge about its orientation with respect to this global coordinate frame through some sensor (e.g., a magnetometer). Note, however, that the UAV has no *a priori* knowledge about its initial position, velocity, or clock errors (bias and drift). The jth SOP is modeled as a stationary transmitter with state vector

$$\boldsymbol{x}_{\mathrm{s}_j} \triangleq \left[\boldsymbol{r}^{\mathsf{T}}_{\mathrm{s}_j},\ \boldsymbol{x}^{\mathsf{T}}_{\mathrm{clk,s}_j}\right]^{\mathsf{T}}, \quad \boldsymbol{x}_{\mathrm{clk,s}_j} \triangleq \left[\delta t_{\mathrm{s}_j},\ \dot{\delta} t_{\mathrm{s}_j}\right]^{\mathsf{T}}$$

where $\boldsymbol{r}_{\mathrm{s}_j} \in \mathbb{R}^2$ is the SOP's planar position and $\delta t_{\mathrm{s}_j} \in \mathbb{R}$ and $\dot{\delta} t_{\mathrm{s}_j} \in \mathbb{R}$ are the SOP's clock bias and drift, respectively. The SOP's states are assumed to evolve according to

$$\boldsymbol{x}_{\mathrm{s}_j}(k+1) = \mathbf{F}_{\mathrm{s}}\boldsymbol{x}_{\mathrm{s}_j}(k) + \mathbf{G}_{\mathrm{s}}\boldsymbol{w}_{\mathrm{clk,s}_j}(k) \tag{11}$$

$$\mathbf{F}_{\mathrm{s}} \triangleq \mathrm{diag}\left[\mathbf{I}_{2\times 2},\ \mathbf{F}_{\mathrm{clk}}\right], \quad \mathbf{G}_{\mathrm{s}} \triangleq \left[\mathbf{0}_{2\times 2} \quad \mathbf{I}_{2\times 2}\right]^{\mathsf{T}}$$

where $\boldsymbol{w}_{\mathrm{clk,s}_j} \in \mathbb{R}^2$ is the process noise vector driving the jth SOP's clock states and is modeled as a zero-mean white noise sequence with covariance $\mathbf{Q}_{\mathrm{clk,s}_j}$, which has the same form as $\mathbf{Q}_{\mathrm{clk,r}}$, except that $S_{\tilde{w}_{\delta t_{\mathrm{r}}}}$ and $S_{\tilde{w}_{\dot{\delta} t_{\mathrm{r}}}}$ are replaced with SOP clock-specific spectra, $S_{\tilde{w}_{\delta t_{\mathrm{s},j}}}$ and $S_{\tilde{w}_{\dot{\delta} t_{\mathrm{s},j}}}$, respectively.

E. Observation Model

The UAV-mounted receiver makes pseudorange measurements on the jth SOPs, which after mild approximations discussed in [68], can be modeled according to

$$\begin{aligned} z_j(k) &= h\left[\boldsymbol{x}_{\mathrm{r}}(k),\ \boldsymbol{x}_{\mathrm{s}_j}(k)\right] + v_j(k) \\ &= \|\boldsymbol{r}_{\mathrm{r}}(k) - \boldsymbol{r}_{\mathrm{s}_j}(k)\|_2 + c \cdot [\delta t_{\mathrm{r}}(k) - \delta t_{\mathrm{s}_j}(k)] + v_j(k) \end{aligned} \tag{12}$$

where c is the speed of light and v_j is the measurement noise, which is modeled as a discrete-time zero-mean white Gaussian sequence with variance σ^2_j. The measurement noise of all SOPs is assumed to be uncorrelated. Subsequently, the covariance matrix $\mathbf{R}$ of the measurement noise vector $\boldsymbol{v} \triangleq [v_a, v_1, \ldots, v_m]^{\mathsf{T}}$ is given by $\mathbf{R} \triangleq \mathrm{diag}[\sigma^2_a, \sigma^2_1, \ldots, \sigma^2_m]$.

F. EKF Model

The anchor SOP state $\boldsymbol{x}_{s_a}$ is assumed to be known at all time. Hence, the EKF estimates the state vector defined by

$$\boldsymbol{x}(k) \triangleq \left[\boldsymbol{x}^{\mathsf{T}}_{\mathrm{r}}(k), \boldsymbol{x}^{\mathsf{T}}_{\mathrm{s}_1}(k), \ldots, \boldsymbol{x}^{\mathsf{T}}_{\mathrm{s}_m}(k)\right]^{\mathsf{T}}$$

using the set of measurements given by $\{\boldsymbol{z}(l)\}^k_{l=0}$, where $\boldsymbol{z}(l) \triangleq [z_a(l), z_1(l), \ldots, z_m(l)]^{\mathsf{T}}$. From (10)–(12), the overall system equations are given by

$$\boldsymbol{x}(k+1) = \mathbf{F}\boldsymbol{x}(k) + \mathbf{\Gamma}\boldsymbol{g}_{\mathrm{r}}\left[\boldsymbol{u}_{\mathrm{r}}(k)\right] + \mathbf{G}\boldsymbol{w}(k) \tag{13}$$

$$\boldsymbol{z}(k) = \boldsymbol{h}\left[\boldsymbol{x}(k)\right] + \boldsymbol{v}(k) \tag{14}$$

$$\begin{aligned}\mathbf{F} &\triangleq \operatorname{diag}\left[\mathbf{F}_{\mathrm{r}}, \mathbf{F}_{\mathrm{s}}, \mathbf{F}_{\mathrm{s}}, \ldots, \mathbf{F}_{\mathrm{s}}\right], \quad \boldsymbol{\Gamma} \triangleq \left[\boldsymbol{\Gamma}_{\mathrm{r}}^{\mathsf{T}}\ \mathbf{0}_{4m\times 2}^{\mathsf{T}}\right]^{\mathsf{T}} \\ \mathbf{G} &\triangleq \operatorname{diag}\left[\mathbf{I}_{6\times 6}, \mathbf{G}_{\mathrm{s}}, \mathbf{G}_{\mathrm{s}}, \ldots, \mathbf{G}_{\mathrm{s}}\right] \\ \boldsymbol{h}\left[\boldsymbol{x}(k)\right] &\triangleq \left[h\left[\boldsymbol{x}_{\mathrm{r}}(k), \boldsymbol{x}_{\mathrm{s}_a}(k)\right], h\left[\boldsymbol{x}_{\mathrm{r}}(k), \boldsymbol{x}_{\mathrm{s}_1}(k)\right], \ldots \right. \\ &\qquad \left. h\left[\boldsymbol{x}_{\mathrm{r}}(k), \boldsymbol{x}_{\mathrm{s}_m}(k)\right]\right]^{\mathsf{T}}\end{aligned}$$

and $\boldsymbol{w}(k)$, defined as

$$\boldsymbol{w}(k) \triangleq \left[\boldsymbol{w}_{\mathrm{r}}^{\mathsf{T}}(k), \boldsymbol{w}_{\mathrm{clk,s}_1}^{\mathsf{T}}(k), \ldots, \boldsymbol{w}_{\mathrm{clk,s}_m}^{\mathsf{T}}(k)\right]^{\mathsf{T}}$$

is a zero-mean white Gaussian vector with covariance

$$\mathbf{Q} \triangleq \operatorname{diag}\left[\mathbf{Q}_{\mathrm{r}}, \mathbf{Q}_{\mathrm{clk,s}_1}, \ldots, \mathbf{Q}_{\mathrm{clk,s}_m}\right].$$

A standard EKF is implemented based on (13) and (14) to produce an estimate $\hat{\boldsymbol{x}}(k|i) \triangleq \mathbb{E}[\boldsymbol{x}(k)|\{\boldsymbol{z}(l)\}_{l=0}^{i}]$, for $i \leq k$, and an associated error covariance $\mathbf{\Sigma}(k|i)$.

IV. MULTIOBJECTIVE MOTION PLANNING STRATEGY

This section defines the motion planning problem and formulates it as a multiobjective optimization problem.

A. Multiobjective Motion Planning Problem Definition

Consider a UAV that has been deployed into a GNSS-denied environment with no *a priori* knowledge of its own states $\boldsymbol{x}_{\mathrm{r}}$. The environment consists of one anchor SOP whose states $\boldsymbol{x}_{\mathrm{s}_a}$ are fully known for all time and m SOPs whose states $\{\boldsymbol{x}_{\mathrm{s}_j}\}_{j=1}^{m}$ are unknown. In order to navigate, the UAV fuses pseudoranges drawn to the SOPs (12) through an EKF to estimate its own states while simultaneously estimating the states of the unknown SOPs, as discussed in Section III. The UAV is tasked with navigating to within a distance d of a waypoint position $\boldsymbol{r}_{\mathrm{t}}$ with probability $(1-\alpha)$, given its EKF-produced UAV position estimate, denoted $\hat{\boldsymbol{r}}_{\mathrm{r}}(k|k)$, and the associated block of the estimation error covariance, denoted $\mathbf{\Sigma}_{\boldsymbol{r}_{\mathrm{r}}}(k|k)$. Formally, this task is achieved when the following is satisfied:

$$\Pr\left[\|\boldsymbol{r}_{\mathrm{r}}(k)-\boldsymbol{r}_{\mathrm{t}}\|_2^2 \geq d^2 \mid \hat{\boldsymbol{r}}_{\mathrm{r}}(k|k),\ \mathbf{\Sigma}_{\boldsymbol{r}_{\mathrm{r}}}(k|k)\right] \leq \alpha. \tag{15}$$

To navigate to the waypoint and satisfy (15), the UAV selects a sequence of acceleration inputs $\boldsymbol{u}_{\mathrm{r}}(k), k = 0, 1, \ldots$. A *naive* strategy is to select these inputs so that the UAV navigates directly toward the waypoint as fast as possible without violating velocity and acceleration constraints 7. However, flying in a straight line in the GNSS-denied environment considered herein, could cause the UAV to miss the waypoint or cause filter divergence altogether. This is due to poor estimability of the UAV's and environment's states.

In this article, a more sophisticated MOMP strategy is developed, where the UAV prescribes its trajectory by balancing two objectives: 1) navigating toward the waypoint; and 2) making strategic maneuvers, which do not necessarily move the UAV toward the waypoint, in order to reduce the UAV's position uncertainty. These objectives will be achieved by formulating a multiobjective optimization problem, which is discussed next.

B. Cost Function Derivation

To formulate the MOMP strategy as an optimization problem, three quantities must be defined: 1) a cost function; 2) an optimization variable; and 3) constraints on the optimization variable. The optimization variable is defined as the input vector $\boldsymbol{u}_{\mathrm{r}}$ of the UAV's acceleration and heading (cf., 3), and the constraints are readily obtained from the UAV's maximum speed and acceleration ratings (cf., 7). In what follows, three cost functions reflecting the multiple objectives are defined via two approaches: 1) probabilistic; and 2) information theoretic.

1) *Probabilistic Approach:* One possible cost function that reflects the desired objective to reach the waypoint can be readily derived from the probability inequality in (15). After dropping the time argument for compactness of notation, applying Markov's inequality to (15) yields

$$\begin{aligned}\Pr\left[\|\boldsymbol{r}_{\mathrm{r}}-\boldsymbol{r}_{\mathrm{t}}\|_2^2 \geq d^2 \mid \hat{\boldsymbol{r}}_{\mathrm{r}}, \mathbf{\Sigma}_{\boldsymbol{r}_{\mathrm{r}}}\right] &\leq \frac{\mathbb{E}\left[\|\boldsymbol{r}_{\mathrm{r}}-\boldsymbol{r}_{\mathrm{t}}\|_2^2\right]}{d^2} \\ &= \frac{\operatorname{tr}(\mathbf{\Sigma}_{\boldsymbol{r}_{\mathrm{r}}}) + \|\hat{\boldsymbol{r}}_{\mathrm{r}}-\boldsymbol{r}_{\mathrm{t}}\|_2^2}{d^2}\end{aligned} \tag{16}$$

where $\operatorname{tr}(\cdot)$ denotes the trace of a matrix. Note that the above inequality assumes that the EKF is unbiased, i.e., $\mathbb{E}[\boldsymbol{r}_{\mathrm{r}} - \hat{\boldsymbol{r}}_{\mathrm{r}}] = \mathbf{0}$. In this case, to satisfy the mission in (15), one needs to minimize the cost function

$$J_{\mathrm{Markov}} \triangleq \operatorname{tr}(\mathbf{\Sigma}_{\boldsymbol{r}_{\mathrm{r}}}) + \|\hat{\boldsymbol{r}}_{\mathrm{r}}-\boldsymbol{r}_{\mathrm{t}}\|_2^2 \tag{17}$$

in the hopes that the right-hand side of (16) becomes less than the desired probability α. The cost function J_{Markov} explicitly shows the two objectives the UAV is trying to balance: 1) mission completion, captured by the term $\|\hat{\boldsymbol{r}}_{\mathrm{r}}-\boldsymbol{r}_{\mathrm{t}}\|_2^2$, which is minimized when the UAV's position estimate is at the target; and 2) uncertainty reduction, captured by the term $\operatorname{tr}(\mathbf{\Sigma}_{\boldsymbol{r}_{\mathrm{r}}})$, which when minimized, ensures that the UAV's true position is as close as possible to the UAV's position estimate when the estimate is at the target.

2) *Information Theoretic Approaches:* Another way to derive a cost function for the MOMP strategy is using information theoretic measures. The EKF produces the estimate $\hat{\boldsymbol{r}}_{\mathrm{r}}$, which, ignoring the effect of nonlinearities and assuming Gaussian noise, is the conditional mean of $\boldsymbol{r}_{\mathrm{r}}$ with the associated estimation error covariance $\mathbf{\Sigma}_{\boldsymbol{r}_{\mathrm{r}}}$. Let $\mathcal{N}_{\mathrm{r}}$ denote the probability density function (pdf) of $\boldsymbol{r}_{\mathrm{r}}$ conditioned on all the measurements, which is given by

$$\mathcal{N}_{\mathrm{r}}: \quad \boldsymbol{r}_{\mathrm{r}} \sim \mathcal{N}\left(\hat{\boldsymbol{r}}_{\mathrm{r}}, \mathbf{\Sigma}_{\boldsymbol{r}_{\mathrm{r}}}\right) \tag{18}$$

where $\mathcal{N}(\boldsymbol{\mu}, \mathbf{\Sigma})$ denotes the multivariate Gaussian pdf with mean $\boldsymbol{\mu}$ and covariance matrix $\mathbf{\Sigma}$. Another way to define the objectives is through a target probability density $\mathcal{N}_{\mathrm{t}}$ defined as

$$\mathcal{N}_{\mathrm{t}}: \quad \boldsymbol{r}_{\mathrm{r}} \sim \mathcal{N}\left(\boldsymbol{r}_{\mathrm{t}}, \epsilon^2\mathbf{I}\right) \tag{19}$$

where ϵ is a small positive number. Equation (19) is saying that it is desired that the UAV's position to be centered at the target with a small uncertainty. A natural approach to achieve this is to minimize the distance between the current and target pdfs. Such distance metrics are commonly used in information theory, such as the Kullback–Leibler (KL) divergence D_{KL} or the 2-Wasserstein metric W_2. For Gaussian distributions such as $\mathcal{N}_{\mathrm{r}}$ and $\mathcal{N}_{\mathrm{t}}$, the KL divergence can be expressed as

$$D_{\mathrm{KL}}\left(\mathcal{N}_{\mathrm{r}} \| \mathcal{N}_{\mathrm{t}}\right) = \frac{1}{2\epsilon^2}\left[\operatorname{tr}\left(\boldsymbol{\Sigma}_{\boldsymbol{r}_{\mathrm{r}}}\right) + \|\hat{\boldsymbol{r}}_{\mathrm{r}} - \boldsymbol{r}_{\mathrm{t}}\|_2^2\right] - \frac{1}{2}\left[\ln\det\left(\boldsymbol{\Sigma}_{\boldsymbol{r}_{\mathrm{r}}}\right) + 2 - 4\ln\epsilon\right] \tag{20}$$

and the 2-Wasserstein metric becomes

$$W_2\left(\mathcal{N}_{\mathrm{r}}, \mathcal{N}_{\mathrm{t}}\right) = \left[\operatorname{tr}\left(\boldsymbol{\Sigma}_{\boldsymbol{r}_{\mathrm{r}}}\right) + \|\hat{\boldsymbol{r}}_{\mathrm{r}} - \boldsymbol{r}_{\mathrm{t}}\|_2^2\right] + 2\epsilon\left[\epsilon - \operatorname{tr}\left(\boldsymbol{\Sigma}_{\boldsymbol{r}_{\mathrm{r}}}^{\frac{1}{2}}\right)\right]. \tag{21}$$

Next, define the cost functions

$$\begin{aligned} J_{\mathrm{KL}} &\triangleq 2\epsilon^2 D_{\mathrm{KL}}\left(\mathcal{N}_{\mathrm{r}} \| \mathcal{N}_{\mathrm{t}}\right) \\ &= J_{\mathrm{Markov}} - \epsilon^2\left[\ln\det\left(\boldsymbol{\Sigma}_{\boldsymbol{r}_{\mathrm{r}}}\right) + 2 - 4\ln\epsilon\right] \end{aligned} \tag{22}$$

and

$$\begin{aligned} J_{\mathrm{W}} &\triangleq W_2\left(\mathcal{N}_{\mathrm{r}}, \mathcal{N}_{\mathrm{t}}\right) \\ &= J_{\mathrm{Markov}} + 2\epsilon\left[\epsilon - \operatorname{tr}\left(\boldsymbol{\Sigma}_{\boldsymbol{r}_{\mathrm{r}}}^{\frac{1}{2}}\right)\right]. \end{aligned} \tag{23}$$

Minimizing J_{KL} is equivalent to minimizing $D_{\mathrm{KL}}(\mathcal{N}_{\mathrm{r}} \| \mathcal{N}_{\mathrm{t}})$ for any value of $\epsilon > 0$, since ϵ is independent of the optimization variable $\boldsymbol{u}_{\mathrm{r}}$. Both J_{KL} and J_{W} are explicitly expressed as J_{Markov} with the addition of constants and terms penalizing the difference between the current and target pdfs. However, it is shown next that for small enough ϵ, all three cost functions are equal up to a small difference δ.

3) *Equivalence of Probabilistic and Information Theoretic Approaches:* It is assumed the mission time is upper bounded by κ time-steps. Next, let $\mathbf{P}_{\mathrm{pv}}(k)$ denote the covariance matrix of $\boldsymbol{x}_{\mathrm{pv}}(k)$, which can be expressed as

$$\mathbf{P}_{\mathrm{pv}}(k) = \begin{bmatrix} \mathbf{P}_{\boldsymbol{r}_{\mathrm{r}}}(k) & \mathbf{P}_{\boldsymbol{r}_{\mathrm{r}}\dot{\boldsymbol{r}}_{\mathrm{r}}}(k) \\ \mathbf{P}_{\boldsymbol{r}_{\mathrm{r}}\dot{\boldsymbol{r}}_{\mathrm{r}}}^{\mathsf{T}}(k) & \mathbf{P}_{\dot{\boldsymbol{r}}_{\mathrm{r}}}(k) \end{bmatrix}$$

where $\mathbf{P}_{\boldsymbol{r}_{\mathrm{r}}}(k)$ and $\mathbf{P}_{\dot{\boldsymbol{r}}_{\mathrm{r}}}(k)$ are the covariance matrices of $\boldsymbol{r}_{\mathrm{r}}(k)$ and $\dot{\boldsymbol{r}}_{\mathrm{r}}(k)$, respectively, and $\mathbf{P}_{\boldsymbol{r}_{\mathrm{r}}\dot{\boldsymbol{r}}_{\mathrm{r}}}(k)$ is the cross-covariance. Moreover, using (5)–(7), and the property $\mathbf{A} \preceq \operatorname{tr}(\mathbf{A})\mathbf{I}$ for any matrix $\mathbf{A} \succeq \mathbf{0}$, $\mathbf{Q}_c(k)$ may be upper bounded as

$$\mathbf{Q}_c(k) \preceq \left(\tilde{q}_a + a_{\mathrm{r,max}}^2\tilde{q}_\theta\right)\mathbf{I}_{2\times 2} \tag{24}$$

where the right-hand side of the inequality is independent of time. It follows from (4) and (24) that

$$\begin{aligned} \mathbf{Q}_{\mathrm{pv}}(k) &\preceq \left(\tilde{q}_a + a_{\mathrm{r,max}}^2\tilde{q}_\theta\right)\begin{bmatrix} \frac{T^3}{3}\mathbf{I}_{2\times 2} & \frac{T^2}{2}\mathbf{I}_{2\times 2} \\ \frac{T^2}{2}\mathbf{I}_{2\times 2} & T\mathbf{I}_{2\times 2} \end{bmatrix} \\ &\triangleq \bar{\mathbf{Q}}_{\mathrm{pv}}. \end{aligned} \tag{25}$$

The following lemma establishes an upper bound on $\mathbf{P}_{\boldsymbol{r}_{\mathrm{r}}}(k)$ for $k = 0, 1, \ldots, \kappa$.

LEMMA IV.1 Consider the system in (3) with $\mathbf{P}_{\mathrm{pv}}(0) \triangleq \operatorname{diag}[\mathbf{P}_{\boldsymbol{r}_{\mathrm{r}}(0)}, \mathbf{P}_{\dot{\boldsymbol{r}}_{\mathrm{r}}(0)}] \succ \mathbf{0}$, then, for $k = 0, 1, \ldots, \kappa$, the following holds:

$$\mathbf{P}_{\boldsymbol{r}_{\mathrm{r}}}(k) \preceq \bar{\mathbf{P}}_{\boldsymbol{r}_{\mathrm{r}}}(k) \tag{26}$$

$$\bar{\mathbf{P}}_{\boldsymbol{r}_{\mathrm{r}}}(k) \triangleq \mathbf{P}_{\boldsymbol{r}_{\mathrm{r}}(0)} + k^2T^2\mathbf{P}_{\dot{\boldsymbol{r}}_{\mathrm{r}}}(0) + \frac{k^3T^3}{3}\left(\tilde{q}_a + a_{\mathrm{r,max}}^2\tilde{q}_\theta\right)\mathbf{I}_{2\times 2}. \tag{27}$$

PROOF From (3), the time-evolution of $\mathbf{P}_{\mathrm{pv}}$ is obtained to be

$$\mathbf{P}_{\mathrm{pv}}(k) = \mathbf{F}_{\mathrm{pv}}^k\mathbf{P}_{\mathrm{pv}}(0)\left(\mathbf{F}_{\mathrm{pv}}^k\right)^{\mathsf{T}} + \sum_{j=0}^{k-1}\mathbf{F}_{\mathrm{pv}}^{k-j-1}\mathbf{Q}_{\mathrm{pv}}(j)\left(\mathbf{F}_{\mathrm{pv}}^{k-j-1}\right)^{\mathsf{T}}. \tag{28}$$

By expanding (28), using (25), using the following properties:

$$\sum_{j=0}^{k-1} j = \frac{k(k-1)}{2}, \quad \sum_{j=0}^{k-1} j^2 = \frac{k(k-1)(2k-1)}{6}$$

and looking at the upper diagonal block of the left- and right-hand sides of (28), (26) is deduced. ■

Now the following theorem establishes equivalence between the three cost functions J_{Markov}, J_{KL}, and J_{W}.

THEOREM IV.1 Consider the system (13), (14), with initial UAV position and velocity prior covariance $\mathbf{P}_{\mathrm{pv}}(0)$, and assume there exists a positive scalar $\underline{p} > 0$ such that

$$\boldsymbol{\Sigma}_{\boldsymbol{r}_{\mathrm{r}}} \geq \underline{p}\,\mathbf{I}_{2\times 2}. \tag{29}$$

Then, over a finite number of time-steps κ, for any $\delta > 0$, there exists an $\epsilon^\star > 0$ such that for $0 < \epsilon < \epsilon^\star$, the following holds:

$$|J_{\mathrm{KL}} - J_{\mathrm{Markov}}| < \delta, \qquad |J_{\mathrm{W}} - J_{\mathrm{Markov}}| < \delta. \tag{30}$$

PROOF The EKF is estimating the posterior estimation error covariance, denoted by $\boldsymbol{\Sigma}_{\boldsymbol{r}_{\mathrm{r}}}(k|k)$. Given the properties of Kalman filters, the following inequality holds:

$$\boldsymbol{\Sigma}_{\boldsymbol{r}_{\mathrm{r}}}(k|k) \preceq \mathbf{P}_{\boldsymbol{r}_{\mathrm{r}}}(k). \tag{31}$$

Moreover, from (27), one can see that $\bar{\mathbf{P}}_{\boldsymbol{r}_{\mathrm{r}}}(k) \preceq \bar{\mathbf{P}}_{\boldsymbol{r}_{\mathrm{r}}}(k+1)$, which implies

$$\bar{\mathbf{P}}_{\boldsymbol{r}_{\mathrm{r}}}(k) \preceq \bar{\mathbf{P}}_{\boldsymbol{r}_{\mathrm{r}}}(\kappa). \tag{32}$$

Let $\zeta(\kappa) \triangleq \operatorname{tr}[\bar{\mathbf{P}}_{\boldsymbol{r}_{\mathrm{r}}}(\kappa)]$. Using the property "$\mathbf{A} \preceq \operatorname{tr}(\mathbf{A})\mathbf{I}$," for a matrix $\mathbf{A} \succeq \mathbf{0}$, and dropping the time argument k for compactness of notation, the following can be deduced:

$$\boldsymbol{\Sigma}_{\boldsymbol{r}_{\mathrm{r}}} \preceq \zeta(\kappa)\mathbf{I}_{2\times 2}. \tag{33}$$

The following inequalities can be derived from (33):

$$\left|\ln\det\boldsymbol{\Sigma}_{\boldsymbol{r}_{\mathrm{r}}}\right| \leq \varphi \tag{34}$$

$$\operatorname{tr}\left(\boldsymbol{\Sigma}_{\boldsymbol{r}_{\mathrm{r}}}^{\frac{1}{2}}\right) \leq 2\sqrt{\zeta(\kappa)} \tag{35}$$

where $\varphi \triangleq \max\{2|\ln\zeta(\kappa)|, 2|\ln\underline{p}|\}$. Subsequently, combining (22) and (34), using the property of the absolute value, the following is deduced:

$$|J_{\mathrm{KL}} - J_{\mathrm{Markov}}| \leq \delta_1(\epsilon) \tag{36}$$

where $\delta_1(\epsilon) \triangleq \epsilon^2(\varphi + 2 + 4|\ln\epsilon|)$. Similarly, combining (23) and (35), another inequality is obtained

$$|J_{\mathrm{W}} - J_{\mathrm{Markov}}| \leq \delta_2(\epsilon) \tag{37}$$

TABLE I
Simulation Settings

Parameter	Value
$\boldsymbol{r}_{\mathrm{t}}$	$[400, 200]^{\mathsf{T}}$
$\boldsymbol{x}_{\mathrm{r}}(0)$	$[0, 0, 0, 0, 100, 10]^{\mathsf{T}}$
$\boldsymbol{x}_{\mathrm{s}_a}$	$[100, 250, 10, 0.1]^{\mathsf{T}}$
$\boldsymbol{x}_{\mathrm{s}_1}$	$[200, -50, 20, 0.2]^{\mathsf{T}}$
$\boldsymbol{x}_{\mathrm{s}_2}$	$[300, 300, 30, 0.3]^{\mathsf{T}}$
$\boldsymbol{x}_{\mathrm{s}_3}$	$[-50, 150, 40, 0.4]^{\mathsf{T}}$
$\hat{\boldsymbol{x}}_{\mathrm{r}}(0 \mid -1)$	$\sim \mathcal{N}[\boldsymbol{x}_{\mathrm{r}}(0), \boldsymbol{\Sigma}_{r}(0 \mid -1)]$
$\hat{\boldsymbol{x}}_{\mathrm{s}_j}(0 \mid -1)$	$\sim \mathcal{N}[\boldsymbol{x}_{\mathrm{s}_j}, \boldsymbol{\Sigma}_{s_j}(0 \mid -1)], \quad j = 1, 2, 3$
$\boldsymbol{\Sigma}_{\mathrm{r}}(0 \mid -1)$	$(5 \times 10^3) \cdot \mathrm{diag}[1, 1, 10^{-2}, 10^{-2}, 1, 10^{-1}]$
$\boldsymbol{\Sigma}_{\mathrm{s}_j}(0 \mid -1)$	$(10^3) \cdot \mathrm{diag}[1, 1, 1, 10^{-1}], \quad j = 1, 2, 3$
$\{h_{0,\mathrm{r}}, h_{-2,\mathrm{r}}\}$	$\{2 \times 10^{-19}, 2 \times 10^{-20}\}$
$\{h_{0,\mathrm{s}_a}, h_{-2,\mathrm{s}_a}\}$	$\{8 \times 10^{-20}, 4 \times 10^{-23}\},$
$\{h_{0,\mathrm{s}_j}, h_{-2,\mathrm{s}_j}\}$	$\{8 \times 10^{-20}, 4 \times 10^{-23}\}, \quad j = 1, 2, 3$
$\{\tilde{q}_a, \tilde{q}_\theta\}$	$\{0.1\ (\mathrm{m/s}^2)^2, 0.004\ (\mathrm{rad})^2\}$
$\mathbf{R}$	$\mathrm{diag}[400, 500, 600, 700]\ \mathrm{m}^2$
$\{v_{\mathrm{r,max}}, a_{\mathrm{r,max}}\}$	$\{20\ \mathrm{m/s}, 5\ \mathrm{m/s}^2\}$
T	$0.1\ \mathrm{s}$
$1 - \alpha$	95%
d	$25\ \mathrm{m}$

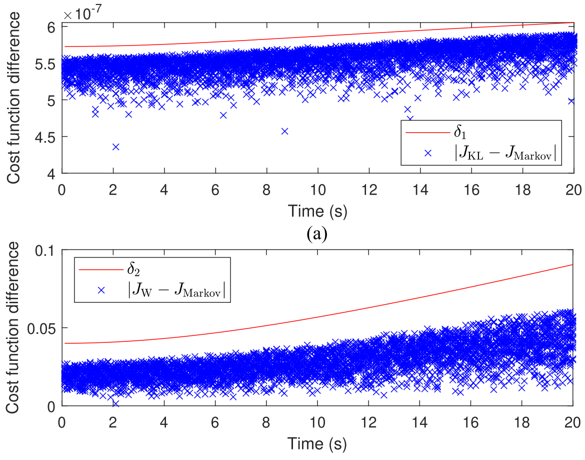

(a)

(b)

Fig. 3. Cost functions equivalence based on the Markov inequality, KL divergence, and Wasserstein metric over time. Illustrated are the difference between (a) the KL divergence and Markov cost functions and (b) Wasserstein and Markov cost functions calculated from the randomly sampled covariance matrix and the established bounds.

where $\delta_2(\epsilon) \triangleq 2\epsilon(\epsilon + 2\sqrt{\zeta(\kappa)})$. One can straightforwardly see that $\delta_1(\epsilon)$ and $\delta_2(\epsilon)$ are strictly increasing functions of $\epsilon > 0$. Consequently, for some $\delta > 0$, one can calculate

$$\epsilon_1 = \delta_1^{-1}(\delta), \quad \epsilon_2 = \delta_2^{-1}(\delta)$$

and define $\epsilon^\star \triangleq \min\{\epsilon_1, \epsilon_2\}$. Therefore, for any $0 < \epsilon < \epsilon^\star$, one can guarantee (30). ■

In order to illustrate Theorem IV.1, Monte Carlo simulations were performed to demonstrate the established bounds (36) and (37). A total of 20 Monte Carlo realizations were generated for each time-step using the simulation settings tabulated in Table I and $\epsilon \equiv 1 \times 10^{-4}$ and $\underline{p} \equiv 1 \times 10^{-4}$. The covariance matrix used to calculate J_{KL}, $\bar{J}_{\mathrm{W}}$, and J_{Markov} were generated based on conditions (26) and (29). At each time-step, the cost function difference was calculated and is plotted in Fig. 3. The covariance matrix had a constant lower bound according to Theorem IV.1 and a time-varying upper bound according to Lemma IV.1. It can be seen that the derived bounds correctly limit the difference between J_{KL} and J_{Markov} and between J_{W} and J_{Markov}.

C. MOMP Optimization Problem

Theorem IV.1 implies that for a small enough target covariance uncertainty, the three cost functions J_{Markov}, J_{KL}, and J_{W} are practically equivalent. Consequently, the MOMP strategy will adopt the cost function $\bar{J}(\boldsymbol{u}_{\mathrm{r}}) \triangleq J_{\mathrm{Markov}}$, constrained to the UAV dynamics, namely

$$\begin{aligned} &\underset{\boldsymbol{u}_{\mathrm{r}}}{\text{minimize}} \quad \bar{J}(\boldsymbol{u}_{\mathrm{r}}) \\ &\text{Subject to:} \quad (8), (13), (14). \end{aligned} \tag{38}$$

The optimization problem (38) does not specify when the mission is completed. A stopping criterion is defined in Section IV-D.

It is desired that the UAV be able to solve the optimization online on its on-board processor. In order to meet this requirement, a greedy approach is adopted, i.e., the optimal control input is computed one step at a time. However, the optimizer could get stuck at a local optimum in which one of the two terms in the cost function dominates. It was observed in simulations that the distance term usually dominates at the beginning, causing the UAV to fly directly toward the waypoint. Once close to the waypoint, the trace of the estimation error covariance starts to dominate, causing the UAV to get stuck flying around the waypoint to minimize its position estimate's uncertainty but to no avail. To avoid such behaviors, the cost function $\bar{J}(\boldsymbol{u}_{\mathrm{r}})$ is reformulated to become a weighted sum given by

$$J(\boldsymbol{u}_{\mathrm{r}}) \triangleq wJ_1[\boldsymbol{u}_{\mathrm{r}}(k)] + (1 - w)J_2[\boldsymbol{u}_{\mathrm{r}}(k)] \tag{39}$$

where $J_1[\boldsymbol{u}_{\mathrm{r}}(k)] \triangleq \|\hat{\boldsymbol{r}}_{\mathrm{r}}(k+1|k) - \boldsymbol{r}_{\mathrm{t}}\|_2^2$, $J_2[\boldsymbol{u}_{\mathrm{r}}(k)] \triangleq \mathrm{tr}[\boldsymbol{\Sigma}_{r_{\mathrm{r}}}(k+1|k+1)]$, and the weight w is changed adaptively. More specifically, J_1 is the Euclidean distance between the UAV's position estimate and the waypoint, which corresponds to the objective of navigating toward the waypoint. Furthermore, J_2 is the A-optimality criterion applied to the UAV's position estimation covariance [32], which corresponds to the objective of minimizing the UAV's position uncertainty. Note that $\boldsymbol{\Sigma}_{r_{\mathrm{r}}}(k+1|k+1)$ can be computed at time-step k since it is independent of the measurements at $k+1$. The MOMP problem is then cast as a greedy motion planning problem to find the optimal input $\boldsymbol{u}_{\mathrm{r}}^*(k)$, that minimizes J subject to the dynamics and $v_{\mathrm{r,max}}$ and $a_{\mathrm{r,max}}$, formally expressed as

$$\begin{aligned} &\underset{\boldsymbol{u}_{\mathrm{r}}(k)}{\text{minimize}} \quad J(\boldsymbol{u}_{\mathrm{r}}) = wJ_1[\boldsymbol{u}_{\mathrm{r}}(k)] + (1 - w)J_2[\boldsymbol{u}_{\mathrm{r}}(k)] \\ &\text{Subject to:} \quad (8), (13), (14) \end{aligned} \tag{40}$$

where the weight is defined as

$$w \triangleq \mathbf{1}(\boldsymbol{\Sigma}_{r_{\mathrm{r}}}, d, \alpha)$$

where $\mathbf{1}(\boldsymbol{\Sigma}_{r_{\mathrm{r}}}, d, \alpha)$ is an indicator function used to switch between each objective and is discussed in Subsection IV-E.

In the next two sections, a test is developed as a stopping criterion for task (15), and the indicator function $\mathbf{1}(\boldsymbol{\Sigma}_{r_{\mathrm{r}}}, d, \alpha)$ is specified.

Note that in practice, a vehicle has constraints on its acceleration and velocity which will also constrain the turning radius of the vehicle. Therefore, as the vehicle approaches the waypoint, it should reduce its velocity in order to make "tighter" turns to successfully reach the waypoint. To this end, an adaptive velocity constraint $v'_{\mathrm{r,max}}$ is proposed, which is defined as

$$v'_{\mathrm{r,max}} = \min\left\{\sqrt{\|\hat{\boldsymbol{r}}_{\mathrm{r}} - \boldsymbol{r}_{\mathrm{t}}\|_2\, a_{\mathrm{r,max}}},\; v_{\mathrm{r,max}}\right\} \tag{41}$$

which is based on the centripetal acceleration. Adjusting the maximum velocity according to (41) will decrease the velocity of the UAV, to ensure that the UAV does not get stuck traversing an infinite loop around the waypoint. Additionally, (41) is effectively a proportional controller, with proportionality constant $\sqrt{a_{\mathrm{r,max}}}$, which has a realistic effect of slowing the UAV down as it approaches the waypoint.

Since the cost function is generally nonconvex, it was solved by an exhaustive search-type algorithm, in order to avoid converging to a local optimum. To this end, the feasible set of maneuvers at time-step t_j was gridded to n_j possible maneuvers. The complexity of evaluating the cost function at a particular input is $\mathcal{O}(1)$ since it is independent of the value of the input. Consequently, the computational complexity at a time-step t_j will be $\mathcal{O}(n_j)$. Of course, advanced numerical optimization solvers can be invoked, which would impact the corresponding computational complexity.

D. Stopping Criterion

Since the UAV does not have access to its true position $\boldsymbol{r}_{\mathrm{r}}$, a test to determine if task (15) is satisfied must be formulated in terms of values the UAV has access to. Specifically, a test is formulated using the UAV's EKF-produced position estimation error covariance $\boldsymbol{\Sigma}_{r_{\mathrm{r}}}$.

THEOREM IV.2 Consider an environment consisting of a UAV that has been deployed into a GNSS-denied environment with no *a priori* knowledge of its own states, one anchor SOP whose states are fully known, m unknown SOPs, and a desired waypoint position $\boldsymbol{r}_{\mathrm{t}}$. Given the distance tolerance from the waypoint d, and the specified confidence probability $1-\alpha$. Then, if

$$1 - F\left(\frac{d^2}{\lambda_{\max}};\; n,\; \sum_{i=1}^{n} b_i^2\right) \leq \alpha \tag{42}$$

holds, then task (15) is satisfied; where $F(\frac{d^2}{\lambda_{\max}};\; n,\; \sum_{i=1}^{n} b_i^2)$ is the cumulative density function (CDF) of a non-central χ^2-distributed random variable with n degrees-of-freedom and noncentrality parameter $\sum_{i=1}^{n} b_i^2$, evaluated at $\frac{d^2}{\lambda_{\max}}$, $\lambda_{\max} \triangleq \max_i \lambda_i(\boldsymbol{\Sigma}_{r_{\mathrm{r}}})$ is the maximum eigenvalue of $\boldsymbol{\Sigma}_{r_{\mathrm{r}}}$, n is the dimension of the UAV position states, and $\boldsymbol{b} = [b_1 \ldots b_n]^{\mathsf{T}}$ is given by

$$\boldsymbol{\Sigma}_{r_{\mathrm{r}}} = \mathbf{U}\boldsymbol{\Lambda}\mathbf{U}^{\mathsf{T}}$$

$$\boldsymbol{b} \triangleq \boldsymbol{\Lambda}^{-\frac{1}{2}}\mathbf{U}(\hat{\boldsymbol{r}}_{\mathrm{r}} - \boldsymbol{r}_{\mathrm{t}}).$$

PROOF The proof will show that (42) is sufficient to satisfy (15). The Euclidean distance term $\|\boldsymbol{r}_{\mathrm{r}} - \boldsymbol{r}_{\mathrm{t}}\|_2^2$ in (15) can be expressed as

$$\begin{aligned}\|\boldsymbol{r}_{\mathrm{r}} - \boldsymbol{r}_{\mathrm{t}}\|_2^2 &= (\hat{\boldsymbol{r}}_{\mathrm{r}} + \tilde{\boldsymbol{r}}_{\mathrm{r}} - \boldsymbol{r}_{\mathrm{t}})^{\mathsf{T}}(\hat{\boldsymbol{r}}_{\mathrm{r}} + \tilde{\boldsymbol{r}}_{\mathrm{r}} - \boldsymbol{r}_{\mathrm{t}})\\ &= (\hat{\boldsymbol{r}}_{\mathrm{r}} + \tilde{\boldsymbol{r}}_{\mathrm{r}} - \boldsymbol{r}_{\mathrm{t}})^{\mathsf{T}}\mathbf{U}^{\mathsf{T}}\boldsymbol{\Lambda}^{-\frac{1}{2}}\boldsymbol{\Lambda}\boldsymbol{\Lambda}^{-\frac{1}{2}}\mathbf{U}(\hat{\boldsymbol{r}}_{\mathrm{r}} + \tilde{\boldsymbol{r}}_{\mathrm{r}} - \boldsymbol{r}_{\mathrm{t}})\\ &= (\boldsymbol{y} + \boldsymbol{b})^{\mathsf{T}}\boldsymbol{\Lambda}(\boldsymbol{y} + \boldsymbol{b})\\ &= \sum_{i=1}^{n} \lambda_i (y_i + b_i)^2\end{aligned} \tag{43}$$

where λ_i is the ith eigenvalue of $\boldsymbol{\Sigma}_{r_{\mathrm{r}}}$, $\boldsymbol{y} \triangleq \boldsymbol{\Lambda}^{-\frac{1}{2}}\mathbf{U}\tilde{\boldsymbol{r}}_{\mathrm{r}} = [y_1 \ldots y_n]^{\mathsf{T}}$ is the estimation error aligned to the coordinates defined by the eigenvectors and eigenvalues of the estimation error covariance matrix; therefore, $\boldsymbol{y} \sim \mathcal{N}(\mathbf{0}_{n\times 1},\; \mathbf{I}_{2\times 2})$. Equation (43) may be upper bounded by replacing all λ_i with $\lambda_{\max}$, which gives

$$\|\boldsymbol{r}_{\mathrm{r}} - \boldsymbol{r}_{\mathrm{t}}\|_2^2 = \sum_{i=1}^{n} \lambda_i (y_i + b_i)^2 \leq \lambda_{\max} \sum_{i=1}^{n} (y_i + b_i)^2. \tag{44}$$

Therefore, an upper bound for the probability in (15) may be established by replacing the Euclidean distance term in (15) by the right-hand side of (44), which gives

$$\Pr\left(\|\boldsymbol{r}_{\mathrm{r}} - \boldsymbol{r}_{\mathrm{t}}\|_2^2 \geq d^2\right) \leq \Pr\left(\lambda_{\max} \sum_{i=1}^{n} (y_i + b_i)^2 \geq d^2\right). \tag{45}$$

Note that $\lambda_{\max} \sum_{i=1}^{n} (y_i + b_i)^2$ is noncentral χ^2-distributed with n degrees-of-freedom and noncentrality parameter $\sum_{i=1}^{n} b_i^2$, yielding the probability

$$\Pr\left(\lambda_{\max} \sum_{i=1}^{n} (y_i + b_i)^2 \geq d^2\right) = 1 - F\left(\frac{d^2}{\lambda_{\max}};\; n,\; \sum_{i=1}^{n} b_i^2\right). \tag{46}$$

Substituting the right-hand side of (46) into (45) yields

$$\Pr\left(\|\boldsymbol{r}_{\mathrm{r}} - \boldsymbol{r}_{\mathrm{t}}\|_2^2 \geq d^2\right) \leq 1 - F\left(\frac{d^2}{\lambda_{\max}};\; n,\; \sum_{i=1}^{n} b_i^2\right). \tag{47}$$

If (42) holds, substituting it into (47) yields (15). ■

E. Indicator Function Selection

The MOMP strategy needs a mechanism to balance the objective functions J_1 and J_2. One way to balance these objectives is to use a function of the uncertainty of the UAV's position estimate as an indicator. If the uncertainty becomes too large, the UAV should focus on decreasing the uncertainty until it becomes small enough so that satisfying task (15) is feasible. Then, the UAV may switch back to navigating toward the waypoint. To make this happen, the indicator function $\mathbf{1}(\boldsymbol{\Sigma}_{r_{\mathrm{r}}}, d, \alpha)$ is set as a necessary condition for (42) to be satisfied. This condition is established in the following lemma.

LEMMA IV.2 A necessary condition for criterion (42) to be satisfied is

$$\eta_\alpha \lambda_{\max} - d^2 \leq 0 \tag{48}$$

where $\eta_\alpha \triangleq F^{-1}(1-\alpha; n, 0)$ is the value of the inverse CDF of a χ^2-distributed random variable with n degrees-of-freedom, evaluated at $1-\alpha$, and n is the dimension of the UAV position states.

PROOF The proof will proceed by contradiction. Assume that (48) is not satisfied, i.e., $\eta_\alpha \lambda_{\max} - d^2 > 0$. Then, from the definition of η_α, the following holds:

$$\frac{d^2}{\lambda_{\max}} < F^{-1}(1-\alpha; n, 0). \tag{49}$$

Since χ^2 CDFs are monotonically increasing, evaluating a n degrees-of-freedom χ^2 CDF at both sides of (49) and moving some terms yields

$$1 - F\left(\frac{d^2}{\lambda_{\max}};\ n,\ 0\right) > \alpha. \tag{50}$$

Note that the CDF of a n degrees-of-freedom noncentral χ^2-distribution decreases as the noncentral parameter increases [69], i.e.,

$$F\left(\frac{d^2}{\lambda_{\max}};\ n,\ c_1\right) \geq F\left(\frac{d^2}{\lambda_{\max}};\ n,\ c_2\right), 0 \leq c_1 < c_2 \tag{51}$$

where c_1 and c_2 are the noncentral parameters. By setting $c_1 = 0$ and $c_2 = \sum_{i=1}^{n} b_i^2 \geq 0$, where b_i are defined according to Theorem IV.2, then (51) implies that

$$1 - F\left(\frac{d^2}{\lambda_{\max}};\ n,\ 0\right) \leq 1 - F\left(\frac{d^2}{\lambda_{\max}};\ n,\ \sum_{i=1}^{n} b_i^2\right). \tag{52}$$

Combining (50) and (52) yields

$$1 - F\left(\frac{d^2}{\lambda_{\max}};\ n,\ \sum_{i=1}^{n} b_i^2\right) > \alpha$$

which is in contradiction with (42). ■

According to Lemma IV.2, the indicator function $\mathbf{1}(\mathbf{\Sigma}_{r_r}, d, \alpha)$ is selected to be

$$\mathbf{1}(\mathbf{\Sigma}_{r_r}, d, \alpha) \triangleq \begin{cases} 1, & \text{if } \eta_\alpha \lambda_{\max} - d^2 \leq 0 \\ 0, & \text{else} \end{cases}. \tag{53}$$

The MOMP strategy is summarized in Fig. 4.

V. SIMULATION RESULTS

This section presents simulation results of a UAV tasked with reaching a waypoint in a GNSS-denied environment, but pseudorange measurements made to unknown SOPs. Three greedy motion planning strategies to prescribe the UAV's trajectory are compared: (i) naive approach, where the UAV moves directly to the waypoint without considering the quality of its position estimate or knowledge of the environment; (ii) MOMP (38), which balances two objectives—minimizing the distance to the waypoint and minimizing UAV position uncertainty; and (iii) adaptive MOMP (40), which is similar to (ii) with the addition of weights to the objectives so that neither one dominates. A Monte Carlo study is conducted using 500 runs to compare each strategy by evaluating the average time to reach the waypoint, final root-mean-squared error (FRMSE) of the UAV's estimated position, final root mean squared distance (FRMSD) toward the waypoint at the end of the mission, and success rate of reaching the waypoint. If the UAV did not reach the waypoint within 200 s, the mission was stopped and recorded as failure.

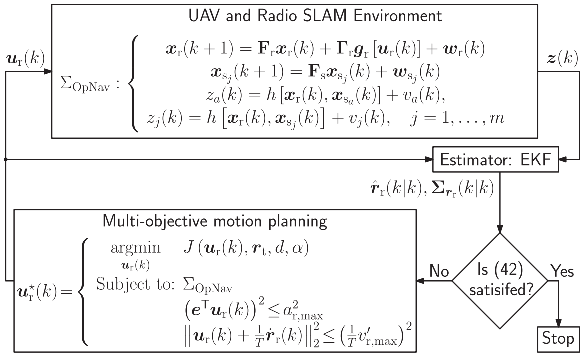

Fig. 4. UAV multiobjective motion planning loop.

A. Simulation Settings

Consider an environment comprising four SOPs and a specified waypoint. The UAV is deployed into an uncertain position, has minimal knowledge of the SOPs in the environment, and is tasked with reaching the known waypoint position $\boldsymbol{r}_{\mathrm{t}}$. The UAV's uncertain deployment position is captured by initializing the EKF with a state estimate, denoted $\hat{\boldsymbol{x}}_{\mathrm{r}}(0|-1)$, with a large estimation error covariance $\mathbf{\Sigma}_{\mathrm{r}}(0|-1)$. One anchor SOP is available, and the remaining three SOPs are unknown, i.e., their initial state estimates $\hat{\boldsymbol{x}}_{\mathrm{s}_j}(0|-1)$ have initial estimation error covariances $\mathbf{\Sigma}_{\mathrm{s}_j}(0|-1) \succ \mathbf{0}_{4\times 4}$, $j = 1, 2, 3$.

The Monte Carlo analysis was conducted over 500 runs. For each run, the EKF was initialized with different initial estimates and used different realizations of process and measurement noise. The EKF and the simulation settings are tabulated in Table I. For each Monte Carlo, run the naive, MOMP, and adaptive MOMP strategies were employed to prescribe the UAV's trajectory according to the closed-loop procedure illustrated in Fig. 4. For each run using the naive strategy, the mission was declared complete by the UAV by checking if $\|\hat{\boldsymbol{r}}_{\mathrm{r}} - \boldsymbol{r}_{\mathrm{t}}\| \leq 5$ m, using d from Table I. For each run using the MOMP strategies, the mission was declared complete according to the stopping criterion described in 4. It is important to note that the nonadaptive MOMP strategy did not declare mission success for any of the runs.

B. Naive and MOMP Strategies Comparison Results

The true and EKF-estimated UAV trajectories, the corresponding final 95th-percentile estimation uncertainty ellipse, the circle around the waypoint with distance d, and the true and estimated SOP positions for an example run is

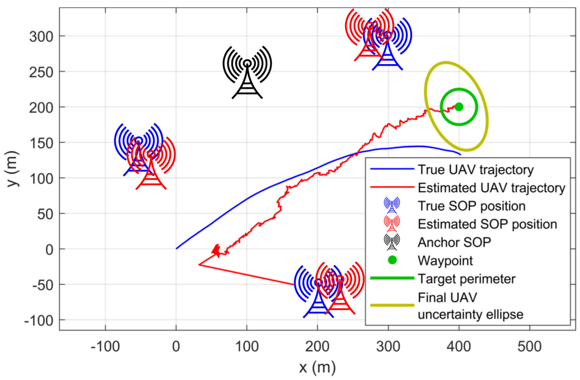

Fig. 5. Results for the naive motion planning strategy. Illustrated are the true and estimated UAV trajectories, true and estimated SOP positions, the waypoint position, the corresponding uncertainty ellipse, and the target perimeter (specified distance *d* to the waypoint). It can be seen that while the UAV actually fails to reach the target perimeter (ground truth trajectory) despite its estimate indicating otherwise.

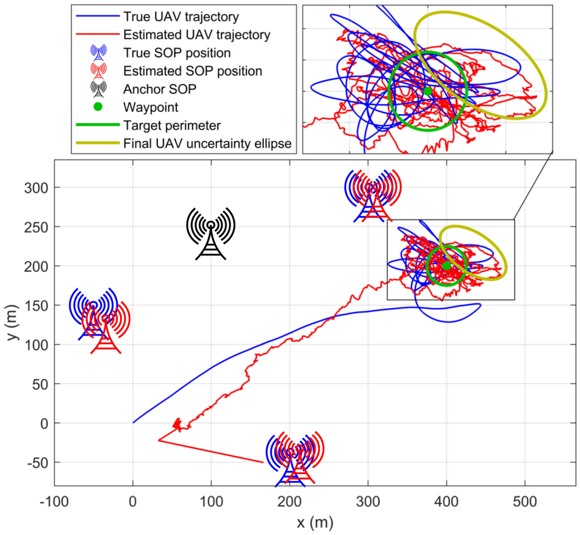

Fig. 6. Results for the MOMP strategy. Illustrated are the true and estimated UAV trajectories, true and estimated SOP positions, the waypoint position, the corresponding uncertainty ellipse, and the target perimeter. The zoomed box in the bottom right illustrates the scenario mentioned in Section IV-C, where the distance term in the cost function dominates at the beginning, causing the UAV to fly directly toward the waypoint. Once close to the waypoint, the trace of the estimation error covariance starts to dominate, causing the UAV to get stuck flying around the waypoint to minimize its position estimate's uncertainty but to no avail.

TABLE II
Motion Planning Performance

Strategy	Time [s]	FRMSE [m]	FRMSD [m]	Success [%]
Naive	27.50	77.04	77.19	36.00
MOMP	200.00	210.38	214.15	32.40
Adaptive MOMP	91.31	18.95	19.32	95.20

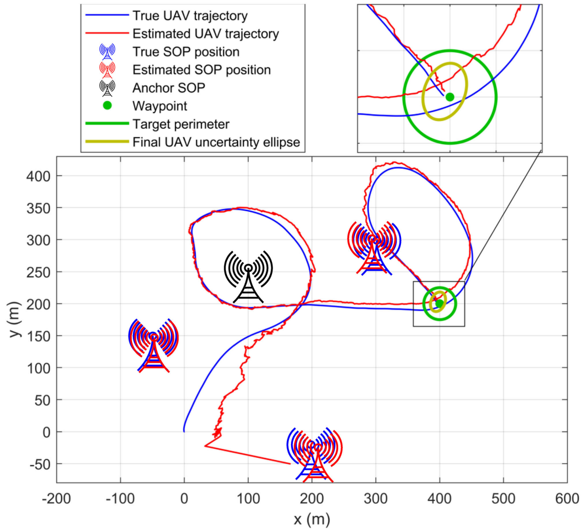

Fig. 7. Results for the adaptive MOMP strategy. Illustrated are the true and estimated UAV trajectories, true and estimated SOP positions, the waypoint position, the corresponding uncertainty ellipse, and the target perimeter. The zoomed box in the bottom right illustrates that the final position uncertainty of the UAV is contained within the target perimeter (i.e., within specified distance *d* to the waypoint).

illustrated in Figs. 5 –7 for the naive, MOMP, and adaptive MOMP strategies, respectively. Table II tabulates the average time-duration to reach the waypoint, the UAV's position FRMSE, the UAV's FRMSD, and the mission completion success rate for the 500 Monte Carlo runs for each strategy. If the UAV did not reach the waypoint within 200 s, the mission was stopped and recorded as failure. The time duration to reach the waypoint is computed by recording the elapsed time from mission start to the time the UAV declares the mission complete. The UAV's position FRMSE is computed by averaging the final position estimation error squared over all runs, and the UAV's FRMSD is computed by averaging the square of the final distance to the waypoint over all the runs. The success rate is computed by dividing the number of runs the UAV's true position was within a distance of *d* from the waypoint by the total number of runs.

The following conclusions can be drawn from these results. First, the nonadaptive MOMP strategy performed the worst in all metrics. The mean time to completion is nearly 200 s, the entire simulation run. The distance term dominates initially causing the UAV to go straight to the target. Once close to the target, the trace term becomes more dominant, causing the UAV to fly around in order to reduce its position uncertainty before heading back to the target. However, because of the poor estimability around the target, the UAV cannot bring its position uncertainty down in the allotted time. In fact, it was observed that the covariance matrix in the EKF tends to grow as the UAV is flying around due to the poor SOP geometry around the target. This causes the UAV to not complete the mission, and explains the large FRMSE and FRMSD values. The FRMSD and the FRMSE of the proposed adaptive MOMP strategy was significantly lower than the naive and nonadaptive MOMP approaches, even if the timeout runs are removed. Second, the naive approach declared an average mission complete time that was about 60 s sooner than the adaptive MOMP strategy.

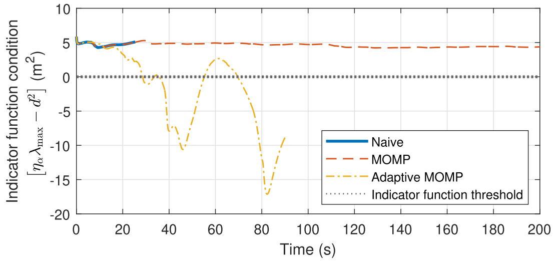

Fig. 8. Indicator function condition (48) for the three strategies: Naive, MOMP, and adaptive MOMP. Illustrated are the values of the indicator function condition over time and the dotted line is the threshold of the switching cost function.

However, only about 30% of these missions were actually successful.

Note that in some runs that used the naive strategy, the filter diverged and the UAV never reached the waypoint, but the filter reported mission completed. This is due to the naive approach failing to consider the uncertainty in the UAV's position estimate, causing the UAV to declare mission complete when the actual position is unacceptably far from the waypoint. This can be seen in Fig. 5, where the UAV position estimate had reached the waypoint, whereas the true UAV position was further than a distance d. In contrast, the UAV spent more time in the adaptive MOMP strategy performing maneuvers around the SOPs before moving to the waypoint, as is illustrated in Fig. 5. The zoomed box of Fig. 7 shows how the MOMP strategy ensures that the uncertainty ellipse corresponding to $1 - \alpha$ is contained within the specified distance d from waypoint before the mission is declared complete. Moreover, this paper does not assume prior knowledge of the UAV's position, velocity, or clock error (bias and drift). Therefore, the initial errors may be very large. This is accounted for by selecting a large initial uncertainty. As the UAV starts moving, its state becomes observable, allowing the EKF to correct some of the large initial errors. As a result, the estimate rapidly converges to the true trajectory's neighborhood, as apparent from Figs. 5–7.

Fig. 8 shows, on one hand, how the indicator function condition (48) indicates adaptive MOMP switching costs to balance information gathering and reaching the waypoint. On the other hand, without the indicator function, the naive and nonadaptive MOMP never meet condition (48), which is necessary for (42), leading to poor performance. These findings demonstrate the tradeoff between mission duration and mission success and stress the importance of considering the UAV's position estimation uncertainty when prescribing the UAV's trajectory.

VI. EXPERIMENTAL RESULTS

This section presents a field experiment demonstrating a UAV navigating to a waypoint using pseudoranges measurements from cellular SOPs. The naive and adaptive MOMP strategies are employed and the resulting performance of each strategy is compared.

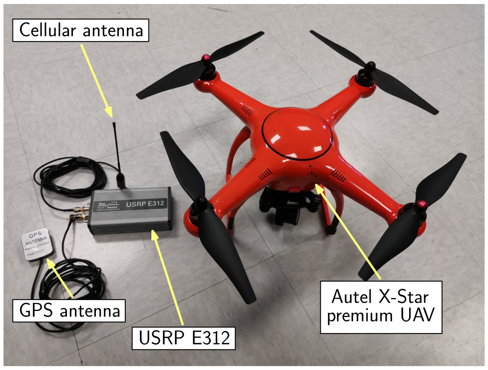

Fig. 9. Experimental setup.

A. Scenario Description

In order to conduct a safe experiment, a postprocessing approach was adopted. To this end, an environment was first built in simulation based on the real field experimental environment. Two simulations were run in this created environment, which corresponded to naive and adaptive MOMP. For each strategy, the UAV was initialized in the same location and was tasked with reaching the same waypoint position. One cellular transmitter was allocated as an anchor SOP and two SOPs were set to be unknown. Next, the produced trajectories for each motion planning strategy were flown manually by a piloted UAV. The SOPs had comparable height, at which the UAV was flown. The piloted UAV true trajectories will serve as the ground truth prescribed trajectories for each strategy. To perform data association, an offline technique was performed, in which the profiles of the pseudoranges were compared with the distance profiles to each SOP. Finally, the pseudoranges were fused through an EKF for each motion planning strategy and the resulting mission performance was compared in terms of mission duration, UAV position rmse, and final distance to the waypoint position.

B. Experimental Setup

An Autel X-Star Premium UAV was equipped with an Ettus universal software radio peripheral (USRP)-E312R to sample cellular CDMA signals. The USRP was tuned to a carrier frequency of 882.75 MHz, which is commonly used by the cellular provided Verizon Wireless. Signals from three cellular SOPs were acquired and tracked via the Multichannel Adaptive Transceiver Information eXtractor (MATRIX) software-defined received (SDR) [70], producing pseudoranges to all SOPs for the entire duration of the flight. A ground truth trajectory for the UAV was parsed from the UAV's onboard navigation system log file, which records position from its integrated GNSS-aided inertial navigation system (INS). The anchor SOP's clock was solved for off-line by subtracting the true distance from the SOP's pseudoranges. The experiment was conducted in Colton, California, USA. The experimental EKF settings are tabulated in Table III, and the experimental setup is shown in Fig. 9.

TABLE III
Experiment Settings

Parameter	Value
$\boldsymbol{r}_{\mathrm{t}}$	$[-21.27, -334.5]^{\mathsf{T}}$
$\boldsymbol{x}_{\mathrm{r}}(0)$	$[-1.6617, -26.98, 0, 0, 0, 0]^{\mathsf{T}}$
$\boldsymbol{x}_{\mathrm{s}_a}$	$[-3762, -2496, 0, -0.8302]^{\mathsf{T}}$
$\boldsymbol{x}_{\mathrm{s}_1}$	$[765.4, 4927, 0, -0.2814]^{\mathsf{T}}$
$\boldsymbol{x}_{\mathrm{s}_2}$	$[380.7, 1611.8, 0, -1.0416]^{\mathsf{T}}$
$\hat{\boldsymbol{x}}_{\mathrm{r}}(0 \mid -1)$	$\sim \mathcal{N}[\boldsymbol{x}_{\mathrm{r}}(0), \boldsymbol{\Sigma}_{r}(0 \mid -1)]$
$\hat{\boldsymbol{x}}_{\mathrm{s}_j}(0 \mid -1)$	$\sim \mathcal{N}[\boldsymbol{x}_{\mathrm{s}_j}, \boldsymbol{\Sigma}_{s_j}(0 \mid -1)], \quad j = 1, 2$
$\boldsymbol{\Sigma}_{\mathrm{r}}(0 \mid -1)$	$(10^4 \cdot \mathrm{diag}[1, 1, 10^{-2}, 10^{-2}, 10^{-4}, 10^{-6}])$
$\boldsymbol{\Sigma}_{\mathrm{s}_j}(0 \mid -1)$	$(10^3 \cdot \mathrm{diag}[1, 1, 10^{-3}, 10^{-5}]), \quad j = 1, 2$
$\{h_{0,\mathrm{r}}, h_{-2,\mathrm{r}}\}$	$\{2 \times 10^{-19}, 2 \times 10^{-20}\}$
$\{h_{0,\mathrm{s}_j}, h_{-2,\mathrm{s}_j}\}$	$\{8 \times 10^{-20}, 4 \times 10^{-23}\}, \quad j = 1, 2$
$\{\tilde{q}_a, \tilde{q}_\theta\}$	$\{0.1\ (\mathrm{m/s}^2)^2, 0.004\ (\mathrm{rad})^2\}$
$\mathbf{R}$	$\mathrm{diag}[400, 400, 400]\ \mathrm{m}^2$
$\{v_{\mathrm{r,max}}, a_{\mathrm{r,max}}\}$	$\{12\ \mathrm{m/s}, 3\ \mathrm{m/s}^2\}$
T	0.1 s
$1 - \alpha$	95%
d	50 m

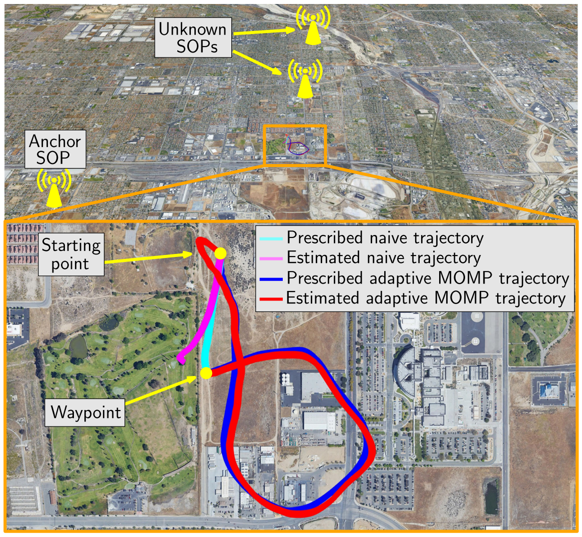

Fig. 10. Experimental environment and UAV trajectories. Prescribed (cyan and blue) and estimated (pink and red) for the naive strategy and the adaptive MOMP strategy. Map data: Google Earth.

TABLE IV
Solutions Performance

Trajectory	Time [s]	2-D RMSE [m]	2-D Final Distance [m]
Naive	57.00	40.23	77.44
Adaptive MOMP	268.9	23.26	12.246

C. Results

The prescribed and estimated UAV trajectories for the naive and adaptive MOMP strategies are illustrated in Fig. 10. The resulting mission performance is tabulated in Table IV. From this table, it can be concluded that using the adaptive MOMP strategy to prescribe the UAV trajectory to navigate to a waypoint resulted in a smaller rmse and final distance to the waypoint compared to using the naive strategy. Note that on one hand, although the naive strategy prescribed the shortest path and declared the mission successful, the UAV's position estimate had large errors, causing the UAV to be unacceptably far from the waypoint, which in turn translates to mission failure. The large errors are attributed to poor prior knowledge of the SOPs in the environment. On the other hand, the adaptive MOMP strategy prescribed a trajectory that performed maneuvers around the environment, which reduced the uncertainty of the SOPs in the environment. The reduction of the uncertainty of the SOP's states simultaneously reduces the uncertainty of the UAV's position states through correlation. Eventually, when the UAV's position estimation error and error covariance are small enough, the UAV switches its objective to navigating toward the waypoint, which is successfully achieved since the filter errors are small.

VII. CONCLUSION

This article developed a MOMP strategy for a UAV navigating to a specified waypoint in a GNSS-denied environment. The UAV was required to reach the waypoint within a specified distance with a specified probability. The UAV only had access to pseudoranges from unknown SOPs, which were used to simultaneously estimate the UAV's states along with the unknown SOPs' states while the UAV navigated to the specified waypoint. The MOMP cost functions were derived in three different approaches—using the Markov inequality, the KL-divergence, and the Wasserstein metric. It was shown that all cost functions are equivalent under certain conditions, and the resulting cost function balanced two objectives: 1) navigate to the waypoint; and 2) reduce UAV position estimation uncertainty. Adaptive weights were introduced to the MOMP cost function to avoid the algorithm getting stuck at local minima. An indicator function was selected, which switches between the two objectives using a function of the UAV's position estimation error covariance. A simple test was derived using the UAV's position estimation error covariance to determine if the UAV had reached the waypoint within the specified distance and a specified confidence probability. Monte Carlo simulations and experimental results demonstrated that the proposed MOMP strategy significantly reduces the UAV's position rmse and the final distance to the waypoint compared to a naive approach, in which the UAV moves directly to the waypoint. The adaptive MOMP strategy also outperformed the naive strategy in terms of mission success rate.

The MOMP strategy studied in this article requires an indicator function to switch between the two components in the cost function, when using greedy motion planning. Future work can extend this framework to adaptive weighting of the two components of the cost function or adopt a receding horizon trajectory optimization strategy to consider both components at the same time. In addition, the cost function of MOMP is generally nonconvex, which upon employing numerical optimization solvers, could result in convergence to local optima, in addition to requiring involved computations which could be infeasible for real-time implementations. Applying a convex information gathering cost (e.g., innovation-based metrics [32]) to MOMP could be the subject of future work.

REFERENCES

[1] T. Ren and M. Petovello
A stand-alone approach for high-sensitivity GNSS receivers in signal-challenged environment
IEEE Trans. Aerosp. Electron. Syst., vol. 53, no. 5, pp. 2438–2448, Oct. 2017.

[2] R. Ioannides, T. Pany, and G. Gibbons
Known vulnerabilities of global navigation satellite systems, status, and potential mitigation techniques
Proc. IEEE, vol. 104, no. 6, pp. 1174–1194, Feb. 2016.

[3] J. Gross, Y. Gu, and M. Rhudy
Robust UAV relative navigation with DGPS, INS, and peer-to-peer radio ranging
IEEE Trans. Aerosp. Electron. Syst., vol. 12, no. 3, pp. 935–944, Jul. 2015.

[4] M. Li and A. Mourikis
High-precision, consistent EKF-based visual-inertial odometry
Int. J. Robot. Res., vol. 32, no. 6, pp. 690–711, May 2013.

[5] A. Soloviev
Tight coupling of GPS, INS, and laser for urban navigation
IEEE Trans. Aerosp. Electron. Syst., vol. 46, no. 4, pp. 1731–1746, Oct. 2010.

[6] H. Feder, J. Leonard, and C. Smith
Adaptive mobile robot navigation and mapping
Int. J. Robot. Res., vol. 18, no. 7, pp. 650–668, Jul. 1999.

[7] H. Durrant-Whyte and T. Bailey
Simultaneous localization and mapping: Part I
IEEE Robot. Autom. Mag., vol. 13, no. 2, pp. 99–110, Jun. 2006.

[8] T. Bailey and H. Durrant-Whyte
Simultaneous localization and mapping: Part II
IEEE Robot. Autom. Mag., vol. 13, no. 3, pp. 108–117, Sep. 2006.

[9] C. Cadena *et al.*
Past, present, and future of simultaneous localization and mapping: Toward the robust-perception age
IEEE Trans. Robot., vol. 32, no. 6, pp. 1309–1332, Dec. 2016.

[10] J. Raquet and R. Martin
Non-GNSS radio frequency navigation
In *Proc. IEEE Int. Conf. Acoust., Speech, Signal Process.*, 2008, pp. 5308–5311.

[11] L. Merry, R. Faragher, and S. Schedin
Comparison of opportunistic signals for localisation
In *Proc. IFAC Symp. Intell. Auton. Veh.*, 2010, pp. 109–114.

[12] Z. Kassas, J. Khalife, A. Abdallah, and C. Lee
I am not afraid of the jammer: Navigating with signals of opportunity in GPS-denied environments
In *Proc. 33rd Int. Tech. Meeting Satell. Division Inst. Navigation*, 2020, pp. 1566–1585.

[13] C. Gentner, T. Jost, W. Wang, S. Zhang, A. Dammann, and U. Fiebig
Multipath assisted positioning with simultaneous localization and mapping
IEEE Trans. Wireless Commun., vol. 15, no. 9, pp. 6104–6117, Sep. 2016.

[14] K. Shamaei, J. Khalife, and Z. Kassas
Exploiting LTE signals for navigation: Theory to implementation
IEEE Trans. Wireless Commun., vol. 17, no. 4, pp. 2173–2189, Apr. 2018.

[15] J. del Peral-Rosado, J. López-Salcedo, F. Zanier, and G. Seco-Granados
Position accuracy of joint time-delay and channel estimators in LTE networks
IEEE Access, vol. 6, pp. 25185–25199, Apr., 2018.

[16] J. Khalife and Z. Kassas
Opportunistic UAV navigation with carrier phase measurements from asynchronous cellular signals
IEEE Trans. Aerosp. Electron. Syst., vol. 56, no. 4, pp. 3285–3301, Aug. 2020.

[17] Z. Kassas, A. Abdallah, and M. Orabi
Carpe signum: Seize the signal – opportunistic navigation with 5G
Inside GNSS Mag., vol. 16, no. 1, pp. 52–57, 2021.

[18] C. Yang, T. Nguyen, and E. Blasch
Mobile positioning via fusion of mixed signals of opportunity
IEEE Aerosp. Electron. Syst. Mag., vol. 29, no. 4, pp. 34–46, Apr. 2014.

[19] L. Chen, O. Julien, P. Thevenon, D. Serant, A. Pena, and H. Kuusniemi
TOA estimation for positioning with DVB-T signals in outdoor static tests
IEEE Trans. Broadcast., vol. 61, no. 4, pp. 625–638, Dec. 2015.

[20] S. Fang, J. Chen, H. Huang, and T. Lin
Is FM a RF-based positioning solution in a metropolitan-scale environment? A probabilistic approach with radio measurements
IEEE Trans. Broadcast., vol. 55, no. 3, pp. 577–588, Sep. 2009.

[21] V. Moghtadaiee and A. Dempster
Indoor location fingerprinting using FM radio signals
IEEE Trans. Broadcast., vol. 60, no. 2, pp. 336–346, Jun. 2014.

[22] R. Landry, A. Nguyen, H. Rasaee, A. Amrhar, X. Fang, and H. Benzerrouk
Iridium next LEO satellites as an alternative PNT in GNSS denied environments–Part 1
Inside GNSS Mag., vol. 4, no. 3, pp. 56–64, May 2019.

[23] Z. Kassas, J. Morales, and J. Khalife
New-age satellite-based navigation – STAN: Simultaneous tracking and navigation with LEO satellite signals
Inside GNSS Mag., vol. 14, no. 4, pp. 56–65, 2019.

[24] F. Farhangian and R. Landry
Multi-constellation software-defined receiver for doppler positioning with LEO satellites
Sensors, vol. 20, no. 20, pp. 5866–5883, Oct. 2020.

[25] M. Orabi, J. Khalife, and Z. Kassas
Opportunistic navigation with doppler measurements from iridium next and orbcomm LEO satellites
In *Proc. IEEE Aerosp. Conf.*, 2021, pp. 1–9.

[26] J. Morales and Z. Kassas
Tightly-coupled inertial navigation system with signals of opportunity aiding
IEEE Trans. Aerosp. Electron. Syst., vol. 57, no. 3, pp. 1930–1948, Jun. 2021.

[27] M. Driusso, C. Marshall, M. Sabathy, F. Knutti, H. Mathis, and F. Babich
Vehicular position tracking using LTE signals
IEEE Trans. Veh. Technol., vol. 66, no. 4, pp. 3376–3391, Apr. 2017.

[28] K. Shamaei and Z. Kassas
LTE receiver design and multipath analysis for navigation in urban environments
Navigation J. Inst. Navigation, vol. 65, no. 4, pp. 655–675, Dec. 2018.

[29] C. Yang and A. Soloviev
Mobile positioning with signals of opportunity in urban and urban canyon environments
In *Proc. IEEE/ION Position, Location, Navigation Symp.*, 2020, pp. 1043–1059.

[30] J. Khalife and Z. Kassas
Precise UAV navigation with cellular carrier phase measurements
Proc. IEEE/ION Position, Location, Navigation Symposium, Apr. 2018, pp. 978–989.

[31] C. Yang and A. Soloviev
Simultaneous localization and mapping of emitting radio sources-SLAMERS
In *Proc. ION GNSS Conf.*, 2015, pp. 2343–2354.

[32] Z. Kassas, A. Arapostathis, and T. Humphreys
Greedy motion planning for simultaneous signal landscape mapping and receiver localization
IEEE J. Sel. Topics Signal Process., vol. 9, no. 2, pp. 247–258, Mar. 2015.

[33] Z. Kassas and T. Humphreys
Receding horizon trajectory optimization in opportunistic navigation environments
IEEE Trans. Aerosp. Electron. Syst., vol. 51, no. 2, pp. 866–877, Apr. 2015.

[34] G. Qian, D. Pebrianti, Y. Chun, Y. Hao, and L. Bayuaji
Waypoint navigation of quad-rotor MAV
In *Proc. IEEE Int. Conf. Syst. Eng. Technol.*, 2017, pp. 38–42.

[35] Y. Saidi, M. Tadjine, and A. Nemra
Robust waypoints navigation using fuzzy type 2 controller
In *Proc. Int. Conf. Adv. Elect. Eng.*, 2019, pp. 1–6.

[36] T. Puls, M. Kemper, R. Küke, and A. Hein
GPS-based position control and waypoint navigation system for quadrocopters
In *Proc. IEEE/RSJ Int. Conf. Intell. Robots Syst.*, 2009, pp. 3374–3379.

[37] M. Imamura, R. Tomitaka, Y. Miyazaki, K. Kobayashi, and K. Watanabe
Outdoor waypoint navigation for an intelligent wheelchair using differential GPS and INS
In *Proc. SICE Annu. Conf.*, vol. 3, 2004, pp. 2193–2196.

[38] R. Tomitaka, K. Kobayashi, and K. Watanabe
Development of intelligent vehicle for waypoints navigation
In *Proc. SICE Annu. Conf.*, vol. 1, 2003, pp. 1094–1097.

[39] S. He, H. Shin, A. Tsourdos, and C. Lee
Energy-optimal waypoint-following guidance considering autopilot dynamics
IEEE Trans. Aerosp. Electron. Syst., vol. 56, no. 4, pp. 2701–2717, Aug. 2020.

[40] I. Whang and T. Hwang
Horizontal waypoint guidance design using optimal control
IEEE Trans. Aerosp. Electron. Syst., vol. 38, no. 3, pp. 1116–1120, Jul. 2002.

[41] T. Davies and A. Jnifene
Multiple waypoint path planning for a mobile robot using genetic algorithms
In *Proc. IEEE Int. Conf. Comput. Intell. Meas. Syst. Appl.*, 2006, pp. 21–26.

[42] J. Petereit, T. Emter, and C. Frey
Safe mobile robot motion planning for waypoint sequences in a dynamic environment
In *Proc. IEEE Int. Conf. Ind. Technol.*, 2013, pp. 181–186.

[43] Z. Yan, J. Li, Y. Wu, and G. Zhang
A real-time path planning algorithm for AUV in unknown underwater environment based on combining PSO and waypoint guidance
Sensors, vol. 19, no. 1, pp. 20–33, Dec. 2018.

[44] M. Ataei and A. Yousefi-Koma
Three-dimensional optimal path planning for waypoint guidance of an autonomous underwater vehicle
Robot. Auton. Syst., vol. 67, pp. 23–32, 2015.

[45] C. Hubmann, J. Schulz, M. Becker, D. Althoff, and C. Stiller
Automated driving in uncertain environments: Planning with interaction and uncertain maneuver prediction
IEEE Trans. Intell. Veh., vol. 3, no. 1, pp. 5–17, Mar. 2018.

[46] K. Berntorp, T. Hoang, and S. Di Cairano
Motion planning of autonomous road vehicles by particle filtering
IEEE Trans. Intell. Veh., vol. 4, no. 2, pp. 197–210, Jun. 2019.

[47] H. Karimi and D. Asavasuthirakul
A novel optimal routing for navigation systems-services based on global navigation satellite system quality of service
J. Intell. Transp. Syst., vol. 18, no. 3, pp. 286–298, May 2014.

[48] A. Nowak
Dynamic GNSS mission planning using DTM for precise navigation of autonomous vehicles
J. Navigation, vol. 70, no. 3, pp. 483–504, May 2017.

[49] S. Ragothaman, M. Maaref, and Z. Kassas
Autonomous ground vehicle path planning in urban environments using GNSS and cellular signals reliability maps: Models and algorithms
IEEE Trans. Aerosp. Electron. Syst., vol. 57, no. 2, pp. 1562–1580, Jun. 2021.

[50] S. Ragothaman, M. Maaref, and Z. Kassas
Autonomous ground vehicle path planning in urban environments using GNSS and cellular signals reliability maps: Simulation and experimental results
IEEE Trans. Aerosp. Electron. Syst., vol. 57, no. 4, pp. 2575–2586, Aug. 2021.

[51] J. Isaacs *et al.*
GPS-optimal micro air vehicle navigation in degraded environments
In *Proc. Amer. Control Conf.*, 2014, pp. 1864–1871.

[52] S. Ragothaman, M. Maaref, and Z. Kassas
Multipath-optimal UAV trajectory planning for urban UAV navigation with cellular signals
In *Proc. IEEE Veh. Technol. Conf.*, 2019, pp. 1–6.

[53] G. Zhang and L. Hsu
A new path planning algorithm using a GNSS localization error map for UAVs in an urban area
J. Intell. Robotic Syst., vol. 94, pp. 219–235, 2019.

[54] A. Shetty and G. Gao
Trajectory planning under stochastic and bounded sensing uncertainties using reachability analysis
In *Proc. ION GNSS Conf.*, 2020, pp. 1637–1648.

[55] M. Maaref and Z. Kassas
Optimal GPS integrity-constrained path planning for ground vehicles
In *Proc. IEEE/ION Position, Location, Navigation Symp.*, 2020, pp. 655–660.

[56] S. Prentice and N. Roy
The belief roadmap: Efficient planning in linear POMDPs by factoring the covariance
Robot. Res., vol. 66, pp. 293–305, 2011.

[57] B. Englot, T. Shan, S. Bopardikar, and A. Speranzon
Sampling-based min-max uncertainty path planning
In *Proc. Conf. Decis. Control*, 2016, pp. 6863–6870.

[58] S. Bopardikar, B. Englot, A. Speranzon, and J. Berg
Robust belief space planning under intermittent sensing via a maximum eigenvalue-based bound
Int. J. Robot. Res., vol. 28, pp. 1609–1626, Jul. 2016.

[59] Y. Elisha and V. Indelman
Active online visual-inertial navigation and sensor calibration via belief space planning and factor graph based incremental smoothing
In *Proc. IEEE/RSJ Int. Conf. Intell. Robots Syst.*, 2017, pp. 2616–2622.

[60] R. Schirmer, P. Biber, and C. Stachniss
Efficient path planning in belief space for safe navigation
In *Proc. IEEE/RSJ Int. Conf. Intell. Robots Syst.*, 2017, pp. 2857–2863.

[61] A. Agha-Mohammadi, S. Agarwal, S. Kim, S. Chakravorty, and N. Amato
SLAP: Simultaneous localization and planning under uncertainty via dynamic replanning in belief space
IEEE Trans. Robot., vol. 34, no. 5, pp. 1195–1214, Oct. 2018.

[62] S. Bopardikar, B. Englot, and A. Speranzon
Multiobjective path planning: Localization constraints and collision probability
IEEE Trans. Robot., vol. 31, no. 3, pp. 562–577, Jun. 2015.

[63] S. Singh and P. Sujit
Landmarks based path planning for UAVs in GPS-denied areas
IFAC-PapersOnLine, vol. 49, no. 1, pp. 396–400, 2016.

[64] B. Irani, J. Wang, and W. Chen
A localizability constraint-based path planning method for autonomous vehicles
IEEE Trans. Intell. Transp. Syst., vol. 20, no. 7, pp. 2593–2604, Jul. 2018.

[65] A. Das, K. Subbarao, and F. Lewis
Dynamic inversion with zero-dynamics stabilisation for quadrotor control
IET Control Theory Appl., vol. 3, no. 3, pp. 303–314, 2008.

[66] X. Li and V. Jilkov
Survey of maneuvering target tracking. Part I: Dynamic models
IEEE Trans. Aerosp. Electron. Syst., vol. 39, no. 4, pp. 1333–1364, Oct. 2003.

[67] J. Morales and Z. Kassas
Stochastic observability and uncertainty characterization in simultaneous receiver and transmitter localization
IEEE Trans. Aerosp. Electron. Syst., vol. 55, no. 2, pp. 1021–1031, Apr. 2019.

[68] Z. Kassas and T. Humphreys
Observability analysis of collaborative opportunistic navigation with pseudorange measurements
IEEE Trans. Intell. Transp. Syst., vol. 15, no. 1, pp. 260–273, Feb. 2014.

[69] Y. Sun, Á. Baricz, and S. Zhou
On the monotonicity, Log-Concavity, and tight bounds of the generalized Marcum and Nuttall q-Functions
IEEE Trans. Inf. Theory, vol. 56, no. 3, pp. 1166–1186, Mar. 2010.

[70] J. Khalife, K. Shamaei, and Z. Kassas
Navigation with cellular CDMA signals – Part I: Signal modeling and software-defined receiver design
IEEE Trans. Signal Process., vol. 66, no. 8, pp. 2191–2203, Apr. 2018.

Yanhao Yang (Student Member, IEEE) received the B.E. degree in mechanical engineering from the South China University of Technology, Guangzhou, China. He is currently working toward the M.S. degree with the Department of Mechanical Engineering, Carnegie Mellon University, Pittsburgh, PA, USA.

He was an Exchange Student with the University of California Irvine, Irvine, CA, USA, and a member of the Autonomous Systems Perception, Intelligence, and Navigation (ASPIN) Laboratory. His research interests include motion planning and unmanned aerial vehicles.

Joe Khalife (Member, IEEE) received the B.E. degree in electrical engineering, the M.S. degree in computer engineering from the Lebanese American University (LAU), Beirut, Lebanon, and the Ph.D. degree in electrical engineering and computer science from the University of California Irvine, Irvine, CA, USA.

He is a Postdoctoral Fellow with the University of California Irvine and member of the Autonomous Systems Perception, Intelligence, and Navigation (ASPIN) Laboratory. From 2012 to 2015, he was a Research Assistant with LAU, and has been a member of the ASPIN Laboratory since 2015. His research interests include opportunistic navigation, autonomous vehicles, and software-defined radio.

Dr. Khalife was the recipient of the 2016 IEEE/ION Position, Location, and Navigation Symposium (PLANS) Best Student Paper Award and the 2018 IEEE Walter Fried Award.

Joshua J. Morales (Member, IEEE) received the B.S. degree in electrical engineering from the University of California, Riverside, Riverside, CA, USA, and the Ph.D. degree in electrical engineering and computer science from the University of California Irvine, CA, USA.

He is a Principal with StarNav LLC, Riverside, CA, USA. Previously, he was a member of the Autonomous Systems Perception, Intelligence, and Navigation (ASPIN) Laboratory, University of California Irvine. His research interests include estimation theory, navigation systems, autonomous vehicles, and cyber-physical systems.

Dr. Morales was the recipient of 2016 Honorable Mention from the National Science Foundation (NSF), and 2018 National Center for Sustainable Transportation (NCST) Outstanding Graduate Student of the Year award.

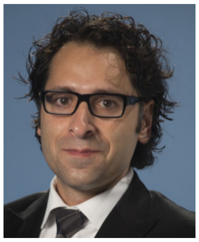

Zaher (Zak) M. Kassas (Senior Member, IEEE) received the B.E. degree in electrical engineering from the Lebanese American University, Beirut, Lebanon, the M.S. degree in electrical and computer engineering from The Ohio State University, Columbus, OH, USA, the M.S.E. degree in aerospace engineering, and the Ph.D. degree in electrical and computer engineering from The University of Texas at Austin, TX, USA.

He is an Associate Professor with the University of California Irvine, CA, USA, and the Director of the Autonomous Systems Perception, Intelligence, and Navigation (ASPIN) Laboratory. He is also the Director of the U.S. Department of Transportation Center: CARMEN (Center for Automated Vehicle Research with Multimodal AssurEd Navigation), focusing on navigation resiliency and security of highly automated transportation systems. His research interests include cyber-physical systems, estimation theory, navigation systems, autonomous vehicles, and intelligent transportation systems.

Dr. Kassas was the recipient of the 2018 National Science Foundation (NSF) Faculty Early Career Development Program (CAREER) award, 2019 Office of Naval Research (ONR) Young Investigator Program (YIP) award, 2018 IEEE Walter Fried Award, 2018 Institute of Navigation (ION) Samuel Burka Award, and 2019 ION Col. Thomas Thurlow Award. He is a Senior Editor for the IEEE TRANSACTIONS ON INTELLIGENT VEHICLES and an Associate Editor for the IEEE TRANSACTIONS ON AEROSPACE AND ELECTRONIC SYSTEMS and the IEEE TRANSACTIONS ON INTELLIGENT TRANSPORTATION SYSTEMS.